7-27-2011

Synthesis and Characterization of Aluminium and Rare-Earth Ion Doped Strontium Ferrite Nanoparticles

Heng Luo

Recommended Citation

Luo, Heng, "Synthesis and Characterization of Aluminium and Rare-Earth Ion Doped Strontium Ferrite Nanoparticles" (2011). *Electronic Theses and Dissertations*. 311.
https://digitalcommons.memphis.edu/etd/311

SYNTHESIS AND CHARACTERIZATION OF ALUMINIUM AND RARE-EARTH

ION DOPED STRONTIUM FERRITE NANOPARTICLES

By

Heng Luo

A Thesis

Submitted in Partial Fulfillment of the

Requirements for Degree of

Master of Science

Major: Physics

The University of Memphis

August 2011

Abstract

Luo, Heng. Master of Science. The University of Memphis. August 2011. Synthesis and Characterization of Aluminium and Rare-Earth Ion Doped Strontium Ferrite Nanoparticles. Major Professor: Dr Sanjay Mishra.

Magnetic materials with high coercive fields, often called permanent magnets, have a wide industrial application ranging from loudspeakers to motors, and sensors. In particular, Strontium hexaferrite $SrFe_{12}O_{19}$ and Barium hexaferrite $BaFe_{12}O_{19}$ have received considerable attention trying to improve their magnetic properties because of their low price per unit of stored energy, which allows large scale production. Other factors such as high Curie temperature, excellent chemical stability, and light weight are associated with them. Many studies have focused on replacing Strontium (Sr) or Iron (Fe) atoms with magnetic and non-magnetic atoms to improve magnetic properties of these ferrites. The studies on Rare-Earth (RE) substituted $SrFe_{12}O_{19}$ are abound. However studies on non-magnetic ion substitution on $SrFe_{12}O_{19}$ are limited. Herein we present a study on the synthesis and characterization of Aluminium (Al) and RE doped $SrFe_{12}O_{19}$.

In this study, Al and RE doped strontium hexaferrite nanoparticles, $SrAl_xFe_{12-x}O_{19}$ and $Sr_{1-x}RE_xFe_{12}O_{19}$ (RE = La, Sm, Gd, Cr) respectively, were synthesized by a combustion sol-gel method. X-ray Diffraction (XRD) results show that with Al^{3+} ions content increasing, the lattice parameters decrease due to smaller Al^{3+} ions replacing Fe^{3+} ions. The substitution also causes the particle shape to change from small spheres to needles at high Al content. This magnetization study

also shows that saturation magnetization at room temperature decreases continuously with Al doping. In particular, particles change from ferromagnet to ferrimagnet. Thermal studies shows that the Curie temperature, also reduces from 470 ℃ to 270 ℃ for $SrFe_{12}O_{19}$ and $SrAl_{10}Fe_2O_{19}$ respectively. More specifically, the coercivity initially increases, reaching a maximum value when Al content x = 2, and then decreases. For $Sr_{1-x}RE_xFe_{12}O_{19}$ (RE = La), when x = 0.25, the doping enhances the magnetic properties.

The Al substitution for iron up to x = 2 bring in fivefold increase in the coercivity with concornitant decrease in magnetization and the Curie temperature as compared to pure $SrFe_{12}O_{19}$. The RE ion doping for Sr, found to improve saturation magnetization of the Sr ferrites. These results are explained on the basis of changes in unit cell volume, site occupancy, and superexchange interaction.

Content

List of Tables

List of Figures

Chapter 1 Introduction

1.1 Classification of Magnetic Materials

Magnetism is a property of materials that indicate how the materials would respond to an applied magnetic field at a microscopic level. Every magnetic material has its own characteristics of orbital movement and electron spins that affect magnetism. So when a magnetic field is applied to the materials, they will have different responses. Upon the basis of responses, magnetism can be classified into five types:

Diamagnetism:

Diamagnetic materials have no net atomic magnetic moments and hence no net magnetism in zero field because all the orbital shells are filled and there are no unpaired electrons.

Paramagnetism:

When an external magnetic field is applied, these magnetic moments will tend to align themselves in the same direction as the applied field, thus reinforcing it.

Ferromagnetism:

A ferromagnet, like a paramagnetic substance, has unpaired electrons. However, in addition to the electrons' intrinsic magnetic moment's tendency to be parallel to an applied field, there is also in these materials a tendency for these magnetic moments to orient parallel to each other to maintain a lowered energy state. Thus, even when

the applied field is removed, the electrons in the material maintain a parallel orientation.

Every ferromagnetic substance has its own temperature, called the Curie temperature, or Curie point, above which it loses its ferromagnetic properties.

Antiferromagnetism:

If the atomic moments of two neighboring sublattices are exactly equal and opposite, the net moment is zero. This type of magnetic ordering is called antiferromagnetism
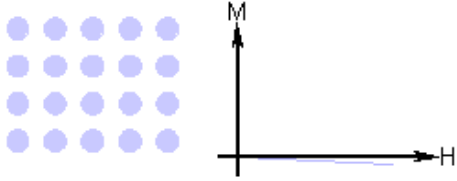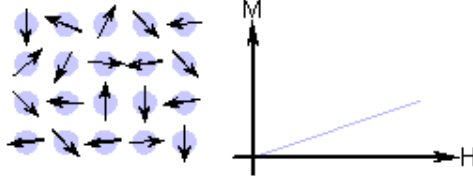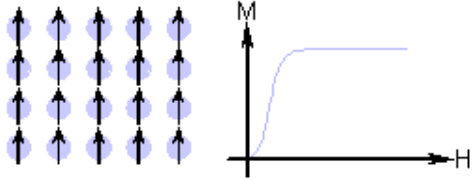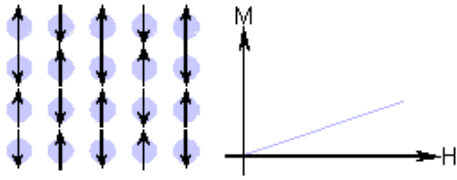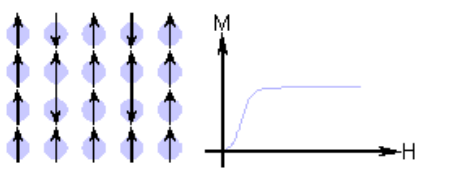
Ferrimagnetism:

If the atomic moments of two neighboring sublattices are not equal then there exists a finite moment. This type of magnetism is called ferrimagnetism. It is similar to ferromagnetism hence it exhibits almost all behavior of ferromagnet but it has very different magnetic ordering. Ferrimagnetic materials are similar to antiferromagnetic materials in which the coupling effect creates an antiparallel alignment of magnetic moments.

Table 1.1 shows the summary of these five magnetisms.

Table 1.1 Summary of magnetism

Types of magnetism	Susceptibility	Atomic & Magnetic Behaviour

Diamagnetism	Small & negative	Atoms have no magnetic moment
Paramagnetism	Small & Positive	Atoms have randomly oriented magnetic moments
Ferromagnetism	Large & Positive	Atoms have parallel aligned magnetic moments
Antiferromagnetism	Small & Positive	Atoms have anti-parallel align magnetic moments
Ferrimagnetism	Large & Positive	Atoms have mixed parallel and anti-parallel aligned magnetic moments

1.2 Permanent Magnets and their Characteristics

Magnetic materials can be classified as either hard or easy materials. The hard magnetic materials are difficult to magnetize and demagnetize, while the soft materials can be magnetized and demagnetized easily. Hard materials have high

coercivity so that they will resist the magnetization action of their own. On the other hand, soft materials are suitable for their application in machines and devices because of their high permeability and their flux multiplying power. The variation of the hysteresis loops is the basic way to describe the difference between these two types of permanent magnets. The hard magnetic materials have a broad hysteresis loop, while the soft magnetic materials show a narrow hysteresis loop. The broad hysteresis loop exhibits that the hard materials can store magnetic energy. The narrow hysteresis loop shows that the soft materials can follow the variation of the applied field without significant loss.

When a magnetic field **H** is applied to ferromagnetic materials it develops a flux density **B** due to orientation of magnetic domains. The relation between **B** and **H** can be represented by the following equation:

$$\boldsymbol{B} = \boldsymbol{\mu_0}(H + M) = \boldsymbol{\mu_0}H + \boldsymbol{J}$$

Where **M** is the magnetization and μ_0 is the permeability of free space equal to $4\pi \times 10^{-7}$ (Tm/A).

The basic parameters to describe a permanent magnet are remanent induction **Br**, the coercive force **Hc**, and the energy product *(BH)max*.

Curie temperature, which is denoted as **Tc**, is another fundamental characteristic used to describe magnetic materials. It is the temperature above which the long range alignment of the atomic dipoles due to exchange energy is totally destroyed and the material gets demagnetized. Therefore, it is desirable to have a higher Curie temperature for the permanent magnetic materials.

1.3 Magnetization and Hysteresis Loops

A hysteresis loop shows the relationship between the induced **B** and the **H**. Ferro- and ferrimagnets exhibit interesting behavior when the field is reduced to zero and then reversed in direction. The graph of *B* (or *M*) versus *H*, which is traced out, is called a Hysteresis loop as shown in Fig. 1.1.
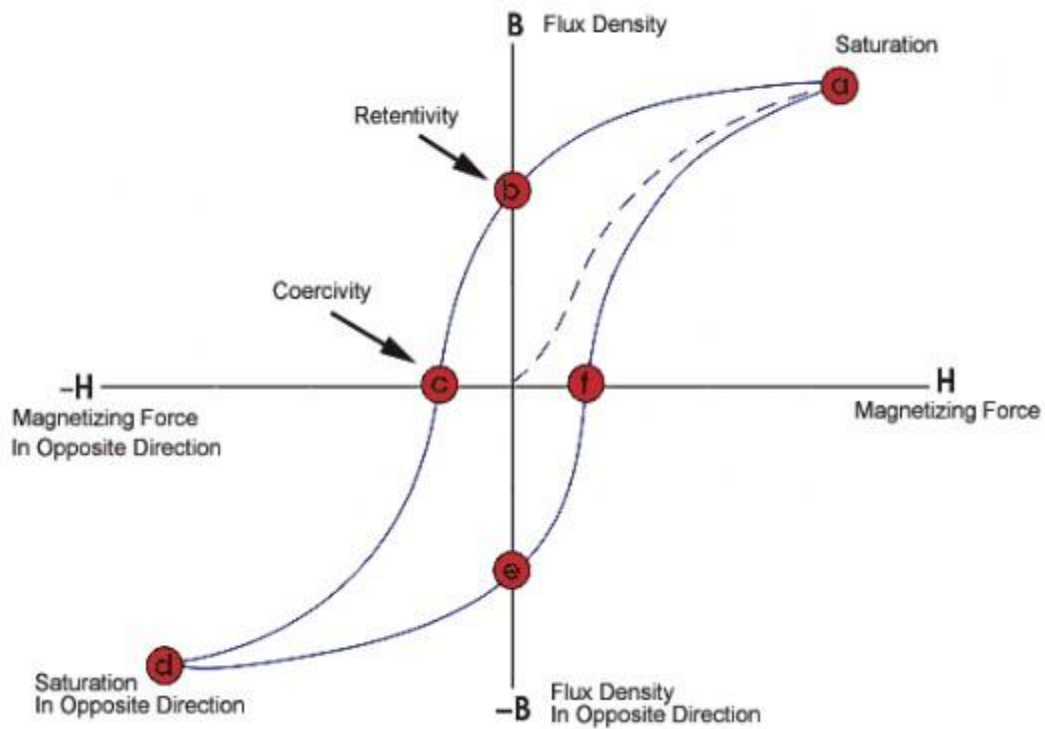
Fig.1.1 Hysteresis loop.

Ferromagnetic materials exhibit parallel alignment of moments that result in large net magnetization even in the absence of magnetic field. Spontaneous and saturation magnetization ,which is **Ms** are the distinct characteristics of ferromagnetic materials. Spontaneous magnetization is the net magnetization that exists inside a uniformly magnetized microscopic volume in the absence of a field. The magnitude

of this magnetization at absolute zero is independent of the spin magnetic moments of electrons. On the other hand, saturation magnetization is the maximum induced magnetic moment that can be obtained in a magnetic field. Beyond this field, no further increase in magnetization can occur. Saturation magnetization is an intrinsic property of the magnetic materials. It is independent of particle size but dependent on the temperature. Due to randomizing effects saturation magnetization becomes zero at a particular temperature, which is T_C. Ferromagnet is in ordered state below T_C. In addition to T_C and M_S, ferromagnet can retain a memory of an applied field once it is removed. This behavior is called hysteresis, and a plot of the variation of magnetization with magnetic field is referred to as a hysteresis loop [1].

1.4 Hexagonal Ferrites

Hexagonal Ferrites are widely used as permanent magnets. They are magnetically hard with special coercivities. They are inexpensive to produce and can be powered and formed easily into any required shape. Hard ferrites have a hexagonal structure and can be classified into following types and respective formulas.

Types of Chemical Formulas

M: $RFe_{12}O_{19}$ R = Ba, Sr, Pb

W: $RMe_{12}O_{16}$ Me = Fe^{2+}, Ni^{2+}, Mn^{2+} etc.

X : $RMe_{12}Fe_{28}$

Y: $R_2Me_2Fe_{12}O_{22}$

Z : $R_3Me_2Fe_{12}O_{41}$

W, X, Y, and Z types are not important economically because of their relatively difficult processing.

1.5 M-Type Ferrites

M-type ferrite has the possible formulas $Sr_{0.6}Fe_2O_3$ (SrM), $Ba_{0.6}Fe_2O_3$ (BaM) and $Pb_{0.6}Fe_2O_3$ (PbM). The M-type ferrites are generally used as permanent magnetic materials because they have higher coercivity. They are preferred over alnicos due to lower material and processing costs as well as superior coercivity. Sr-Ferrite and Ba- Ferrite [40] are the two main materials in the M-type ferrites family. These ferrites have moderate magnetic properties, and their price per unit of available magnetic energy is the lowest.

1.6 Crystal Structure, Magnetic Structure and Phase Diagram of M-type Ferrite

The crystal structure of M-type was determined by Adelskold in 1938 [2]. Fig. 1.2 shows the unit cell of Strontium hexaferrite. The crystal structure consists of two formula units. Its symmetry is characterized by the space group P63/*mmc*. In the unit cell, the O^{-2} ions form a hexagonal close packed lattice. Every five oxygen layers, one O^{-2} ion is replaced with Sr due to the similarity of their ionic radii. The structure is built up from a smaller unit: a cubic block S, having the spinal structure and a hexagonal block R, containing Sr^{+2} ions. Five oxygen layers make one molecule, and two molecules make one unit cell. Each molecule shows 180 degrees

rotational symmetry around the hexagonal *c*-axis against the lower or upper molecule. The O^{-2} layer containing Sr^{+2} is a mirror plane being perpendicular to the *c*-axis. Fe^{+3} ions occupy interstitial positions at different crystallographic sites (i.e., tetrahedral, octahedral and hexahedral sites of oxygen lattice). Table 1.2 shows the crystallographic properties of M- type ferrite.

Table 1.2 Crystallographic properties of M- type ferrite [3].

Paremeter		BaM	SrM	PbM
	Ferrite(s)			
Lattice Constant (mm)	a	0.5893	0.588	0.588
	c	2.3194	2.307	2.302
Molecular wt.		1112	1062	1181
Density gm/cc		5.28	5.11	5.68

M-type compounds have a typical ferromagnetic structure. The magnetism of $SrFe_{12}O_{19}$ comes from the ferric iron, each carrying a magnetic moment of $5\mu B$. These are aligned to give either parallel or anti parallel ferromagnetic interaction. Ions of the same crystallographic position are aligned parallel and this constitutes a magnetic sublattice. The interaction between neighboring ions of different sublattices is a result of super exchange by an oxygen ion. The theory predicts that the atomic moments are parallel when the $Fe - O - Fe$ angle is about $180°$ and antiparallel when this angle is about $90°$. In Fig.ure 1.3, S block contains four Fe^{+3} of up spin in octahedral sites and two Fe^{+3} of down spin in tetrahedral sites. In R block there are three Fe^{+3} of up spin in octahedral sites, two Fe^{+3} of down spin in octahedral sites and one Fe^{+3} of up spin in a trigonal bipyramid site. The exchange scheme of

the compound is shown in Fig. 1.2. The number of ions, their co-ordination, and their

direction of spin orientation for the five iron sub lattices have been given in Table 1.3.

The total magnetization at temperature T can be expressed as:

$$J_s(T) = 6\sigma_k(T) - 2\sigma_{f1}(T) - 2\sigma_{f2}(T) + \sigma_b(T) + \sigma_a(T) \quad\quad (1)$$

Where σ_k, σ_{f1}, σ_{f2}, σ_b and σ_a represent the magnetization of one Fe^{+3} ion in

each sublattice. Because Fe^{+3} has a magnetic moment of 5μB at 0 K, the net

magnetic moment calculated at 0 K is 20 μB for each unit cell.
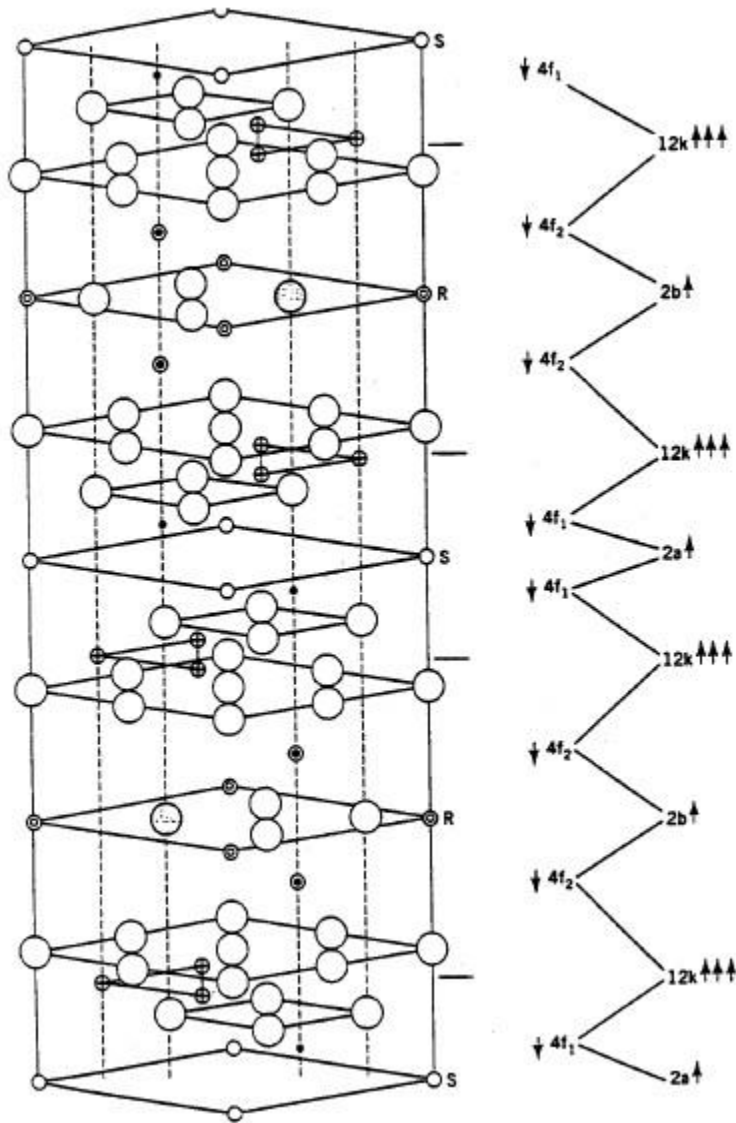
Fig. 1.2 The schematic structure (left) of the hexaferrite $SrFe_{12}O_{19}$. The large open circles are oxygen ions, the large broken circles are Sr ions; small circles with a cross inside represent Fe ions at 12k, small circles containing a filled circle inside represent Fe ions at $4f_2$, small unfilled circles represent Fe ions at $4f_1$, filled small circles represent Fe ions at 2a and small circles with a unfilled circle inside represent Fe ions at 2b. The magnetic structure suggested by Gorter is shown on the right, where the arrows represent the direction of spin polarization [4].

Table 1.3 Number of ions, co-ordinate and spin orientation in the five iron sub lattice of $MFe_{12}O_{19}$ (M = Sr, Ba, Pb)

Sub lattice	Co-ordination	Number of ions	Spin
12k	Octahedral	6	Up
$4f_1$	Tetrahedral	2	Down
$4f_2$	Octahedral	2	Down
2a	Octahedral	1	Up
2b	Fivefold (Triagonal)	1	Up

1.7 Intrinsic Magnetic Properties of M-Type Ferrite

The intrinsic magnetic properties are classified as either primary or secondary. The primary properties, such as saturation magnetization J_s and magnetocrystalline anisotropy constant K_1, are directly related to the magnetic structure. The secondary magnetic properties, such as anisotropy field strength H_A and the specific domain wall energy (γ_w), are derived from the primary properties. The primary and secondary magnetic properties are shown in Table 1.4.

Table 1.4 Primary and secondary magnetic properties of SrM

Primary Properties	
Saturation Magnetization, mT	475
Anisotropic constant, kJ/m^3	360
Curie Temperature, K	750
Secondary Properties	
Specific wall energy, J/m^2	54.2×10^{-4}
Anisotropy field H_A, kA/m	1506
Max coercivity, $(H_c)_{max}$ kA/m	1240

The saturation magnetization, J_s is the maximum magnetic moment per unit volume per gram. It is easily derived from the spin conFig.uration of the sublattices. Eight ionic moments equaling 40 µB per unit cell, which corresponds to 668 mT at 0 K.

The magnetization is strongly bound to the hexagonal c-axis, owing to spin orbit coupling of Fe ions, in particular on the *2b* sites [5]. The direction of the spontaneous magnetization of a hexagonal crystal is expressed by the polar co-ordinates θ and ϕ with respect to crystal axis. Furthermore, assuming that the z axis is the hexagonal axis, the magnetocrystalline anisotropy *E* is given by:

$$E = K_1 Sin^2\theta + K_2 Sin^4\theta + K_3 Sin^6\theta + \cdots\cdots \qquad (2)$$

The energy involved in this process is characterized by the anisotropy constant K_1. The values of higher order constants *(K_2, K_3)* are negligibly small.

The secondary magnetic properties characterize the actual magnetic state. The latter minimizes the three energies involved: the exchange energy *Ee*, the anisotropy energy *Ea*, and the magnetostatic energy *Em*, which are characterized by the value of exchange energy coefficient *A*, anisotropic constant *K,* and saturation magnetization J_s respectively. The secondary magnetic properties for Strontium ferrite are given in Table 1.4.

The specific wall energy γ_w represents a combination of both *Ee* and *Ea*. The critical diameter for single domain behavior, *Dc*, is the diameter below which the magnetic domains are unfavorable in an isolated spherical particle. Although M-ferrite particles are not spherical, magnetostatic interaction between the particles

also play a role. ***Dc*** remains an important indicator for the grain size needed in high quality magnets. In the absence of these domains, magnetization reversal proceeds rotation. The ratio ***Ea/Em*** determines the rotation magnetism. For M-type ferrites where Ea/Em> 0.36, rotation is completely coherent.

The anisotropic field strength H_A is the maximum internal field strength needed for magnetization reversal by coherent rotation. The maximum coercivity ***Hc(max)*** corresponds to H_A, but refers to the external field. It is the reversal field necessary to coerce the material back to zero induction. It explicitly takes into account self demagnetization field of the crystal (NJ_s/μ_0) as governed by the self demagnetization factor ***N***. The latter ranges from 0 (for needles) to 1 (for thin plates). For platelet shaped M-type ferrite crystal ***N*** ranges 0.6 to 0.9. ***Hc(max)*** represents an upper limit for the coercivity of unaligned assembly of non interacting crystals, just as 0.48 ***Hc(max)*** does the same for an isotropic assembly. Real coercivity values are much smaller resulting from the formation of transient domains and magnetostatic interactions.

1.8 Doped M-type Ferrite

Since the discovery of the M-type $BaFe_{12}O_{19}$ and $SrFe_{12}O_{19}$ hexagonal ferrites, numerous studies have been made in the last 10 years to improve their magnetic properties. The magnetic properties of hexaferrites may vary in wide ranges by substitution of divalent or trivalent ions that affects their yus in various devices and instruments. These substitutions are related to the increase of the intrinsic magnetic

properties of the modified M-type phase, in particular to a drastic change of the magneto-crystalline anisotropy field [6].

An variation in the intrinsic magnetic properties of the M-type hexaferrite can be obtained by using optimization of synthetic parameters and partial substitutions for Sr or Fe sites, or both. For Sr sites, metal ions having much larger ionic radii compared with the Fe ion radius, such as La, Sm, and Gd can be used for enhancing the magnetization and coercive field and also they can be used as inhibition agents of the grain growth mechanism at high temperature [7, 8]. The improvement is largely associated with the increase of both magnetocrystalline anisotropy and coercive field as well as the magnetization. For Fe sites, metal ions having the similar size compared with the Fe ion radius, such as Al and Sn can be doped. The doping will not only change the magnetization and coercive field, but also change the color, particle size and the Curie temperature.

Chapter 2 Literature Review

2.1 Historical Development of M-type Ferrite

The magnetite (Fe_3O_4) which is also known as loadstone is the earliest ever known magnet and was used for navigational purpose. Afterwards steel containing some chromium and tungsten were developed. However, the value of coercivity could not increase more than 6 kA/m. In 1917, Japanese introduced Honda Steel which contains 36% of cobalt exhibiting coercivity value of 20 kA/m. The low coercivity in all these martensitic magnetic steels is due to the difficulties in domain boundary movement, resulting from the combined effect of non magnetic inclusions, lattice defects or voids. The major drawback of these materials was instability of permanent magnetic properties due to the aging and demagnetization influence of vibration, mechanical effects and weak magnetic fields [9].

In 1932 the discovery of precipitation hardened Al-Ni-Fe alloys took place. In 1940 the Al-Ni-Co (alnico) was developed [3]. Alnicos are the alloy of Al, Ni, Co and Fe having minor additive of other elements. It was the first magnets to be designated as permanent, because of their resistance to stray magnetic fields, mechanical shocks and elevated temperatures. These materials showed an energy product value of 60-70 kJ/m^3. However, they largely suffered from the scarcity and irregular supply of the cobalt affecting its production adversely.

The basic discovery that magnetoplumbite could be used as a permanent magnet was made by Kato and Takei in the late 1930s [10]. The real breakthrough took place in 1950s

with the development of isotropic barium ferrite as a commercial magnetic material, by Philips Company in Netherland which has nominal composition of $Ba_{0.6}Fe_2O_3$ [11]. The first anisotropic barium ferrite magnet was prepared in 1952 by compacting the powder in a magnetic field [12, 13]. Barium ferrite is mostly used for magnetic tape recording due to its platelets type of crystallite shape with the preferred axis normal to the wide surface and its low coercivity.

Strontium ferrite powder has been manufactured by various processing routes e.g. chemical coprecipitation [14], hydrothermally and sol-gel methods etc. and studies of their magnetic properties have been carried out by various researchers [15,16].

2.2 Strontium Hexagonal Ferrites

In 1988 X. Obradors et al. studied the crystal structure of $SrFe_{12}O_{19}$ by the flux method using $NaFeO_2$ as solvent [17]. They found that structural isomorphism does indeed exist among $BaFe_{12}O_{19}$ and $SrFe_{12}O_{19}$ hexagonal ferrites. However, they anticipate some clues concerning the different crystallochemical behavior of Ba and Sr hexagonal ferrites. It is likely that the structural distortions observed in the metallic polyhedra surrounding the Sr polyhedron are significant enough to modify. It means the relative sublattice preference of substituting ions such as Al^{3+} [18].

In 2003 Fang et al. learned the magnetic and electronic properties of Strontium hexaferrite $SrFe_{12}O_{19}$ [4]. The calculated results, including lattice energy differences to the ferromagnetic ordering, total magnetic moments, conducting behavior are listed in Table 2.1.

Table 2.1 Behavior for different spin configurations. Energies are given with respect to the ferromagnetic ordering [4].

Spin direction of Fe ions in $SrFe_{12}O_{19}$					Energy diff. (eV/unitcell)	Moments (μ_B/unitcell)	Status
2a	2b	4f1	4f2	12k			
+	+	+	+	+	0.000	117.33	Metallic
−	+	+	+	+	−1.44	97.18	Metallic
+	−	+	+	+	−1.89	98.89	Metallic
+	+	−	+	+	−3.80	78.14	Metallic
+	+	+	−	+	−4.89	80	Semiconducting
+	+	+	+	−	−6.88	−0.10	Metallic
−	−	+	−	+	−5.51	40	Semiconducting
+	+	−	−	+	−8.66	40	Semiconducting

They got the information showed that the charge of the Fe ions is close to +3. Local moments for the Fe ions are about $5\mu_B$. The total magnetic moment is 40 μ_B/unit cell, indicating $S = 5/2$ (high spin) for every Fe ion. The oxygen ions have a charge close to −2. Therefore, the ionic model for this ferrite is valid to a first approximation. Magnetic ordering has a strong influence on the electronic structure, while the spin-polarization splitting is almost constant.

In 2004 Wang et al. synthesized nanowires of $SrFe_{12}O_{19}$ with diameters of ~100nm and lengths of ~2.5μm [19]. It was made in a hydrothermal cell at 180℃ with an 0.35 T magnetic field applied. They compared the growth with that under zero magnetic field. The XRD showed that both of the two processes affected in the formation of $SrFe_{12}O_{19}$ while the TEM indicated that the morphology of the particles changed from flake-like in zero magnetic field into nanowires in a magnetic field.

2.3 Doped Strontium Hexagonal Ferrites

In 2007 Shirtcliffe et al. did the research on Al doped barium and Strontium ferrite nanoparticles [14]. The samples were prepared by citrate auto-combustion synthesis. They found that around half of the iron could be substituted for Al in the barium ferrite with structure retention, whereas Strontium aluminium ferrites could be made with any Al content including total substitution of the iron. The samples show the structural and morphological changes as the Al was substituted in the Strontium hexagonal ferrites.

In 2008 Lechevallier et al. did the research on the solubility of rare-earth ion in M-type $SrFe_{12}O_{19}$ hexaferrite [6]. They made $Sr_{1-x}RE_xFe_{12}O_{19}$ and $Sr_{1-x}RE_xFe_{12-x}Co_xO_{19}$ (x = 0 -- 0.4 and RE = Pr, Nd) M-type hexaferrite powder by a conventional ceramic process. They found that only light rare-earth ion can enter the M-type structure, with a solubility that is related to the shape of the 4f electronic charge distribution and to its surroundings in the crystal structure. Rare-earth ions are located in the Sr^{2+} site while Co^{2+} ions modify the surroundings of Sr^{2+} site, increasing the solubility of rare-earth ions.

In the same year Jalli et al. studied the magnetic and microwave properties of Sm-doped $SrFe_{12}O_{19}$ single crystals [20]. The samples was grown from melts using a flux system of $SrCO_3$ and Na_2CO_3. They found that the saturation magnetization and anisotropy field are greatly affected by the doping concentration of Sm. A saturation magnetization (σ_s) of 69.8 emu/g and an anisotropy field (H_k) of 25kOe was achieved.

In 2010 Anterpreet et al. learned the electrical and magnetic properties of rare-earth ion substituted Strontium hexaferrites [21]. They substituted La, Nd, Sm by a standard ceramic processing technique. They achieved the results that AC electrical conductivity increases with increasing frequency, which can be explained on the basis of Koops Model. The values of the magnetization moment (Ms), and remenance (Mr) decrease with increasing rare-earth ions substitution for all the samples. The reason for the decrease may be both the magnetic dilution and spin canting [22], which promotes reduction of superexchange interaction of RE ions. The enhancement of Hc values may be due to higher magnetocrystalline anisotropy.

Chapter 3 Experimental

3.1 The Objectives of the Project

Strontium hexaferrite $SrFe_{12}O_{19}$ have attracted much attention for several years dje to their high permeability and low conductive losses [26]. Though there were a lot of research on $SrFe_{12}O_{19}$, studies on the substituted $SrFe_{12}O_{19}$, particularly on the Re ions and non-magnetic ions doped $SrFe_{12}O_{19}$ were limited.

Objectives:

1. To investigate synthesis approach for the formation of pure phase

   $SrFe_{12}O_{19}$.

2. To study the effect of RE (RE = La, Sm, Gd) ions and Al^{3+} on the magnetic

   properties of ferrites.

   → Substitution of RE ion for Sr is expected to change magnetic anisotropy

   bringing magnetization enhancement.

   → Substitution of Al^{3+} ion for Fe^{3+} ion is expected to change unit cell

   volume because of differences in ionic radii of the two ions. Change is

   expected to affect superexchange interaction between Fe^{3+} ions and thus may

   affect the magnetic properties of ferrites.

3. To study the structural, thermal, and Magnetic characterization of the

   synthesized ferrites

To pursue above objectives we decided to make following sets of samples:

(a) Pure $SrFe_{12}O_{19}$

(b) Al doped $SrAl_xFe_{12-x}O_{19}$ (x = 0, 2, 4, 6, 8, 10, 12)

(c) RE (RE = La, Sm, Gd) ion doped $SrFe_{12}O_{19}$

(d) La ion doped $Sr_{1-x}La_xFe_{12}O_{19}$ (x = 0.1, 0.15, 0.2, 0.25, 0.3)

3.2 Synthesis

All the samples were synthesized by citrate auto-combustion synthesis. We mix the precursor materials in solution as salts during the early stages of the reaction process. Then the mixed precursors can be prepared by co-precipitation or sol–gel processing. Citrate gels containing metal nitrates burn when ignited. The resulting powder can be calcined to form the hexa-ferrite phase.

Synthesis of Pure and Al doped $SrAl_xFe_{12-x}O_{19}$

The raw material used in the research were $Sr(NO_3)_2$ (Sigma-Aldrich), $Fe(NO_3)_3 \cdot 9H_2O$, $Al(NO_3)_3 \cdot 9H_2O$ (purity 99.997% Sigma-Aldrich), Citrate acid($C_6H_8O_7 \cdot H_2O$ Sigma-Aldrich) and NH_4OH. The composition of the sample was taken according to reaction equation given below:
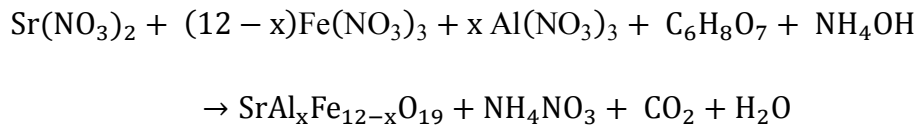
$$Sr(NO_3)_2 + (12-x)Fe(NO_3)_3 + x\,Al(NO_3)_3 + C_6H_8O_7 + NH_4OH$$

$$\rightarrow SrAl_xFe_{12-x}O_{19} + NH_4NO_3 + CO_2 + H_2O$$

Table 3.1 Details of the chemical used in the synthesis for Al doping

Al content (x)	Weight of $Sr(NO_3)_2$/g	Weight of $Fe(NO_3)_3 \cdot 9H_2O$/g	Weight of $Al(NO_3)_3 \cdot 9H_2O$/g	Weight of Citrid acid/g
0	0.1284	2.7876	0	1.5750
2	0.1284	2.3230	0.4313	1.5750
4	0.1284	1.8584	0.8625	1.5750
6	0.1284	1.3938	1.2938	1.5750
8	0.1284	0.9292	1.7250	1.5750
10	0.1284	0.4646	2.1563	1.5750
12	0.1284	0	2.5875	1.5750

Stoichiometric amounts of $Sr(NO_3)_2$, $Fe(NO_3)_3 \cdot 9H_2O$, $Al(NO_3)_3 \cdot 9H_2O$ were dissolved in a minimum amount of deionised water (100 ml for 0.1 mol of Fe3+) by stirring on a hotplate at 60 ℃. It is better to set up the ratio of iron and aluminium to Strontium at 11.5 [27]. Citric acid was dissolved into the solutions to give a molar ratio of metal ions to citric acid of 1:1. Table 3.1 shows the weight details of the chemical used. Then the solutions were allowed several minutes to cool down to room temperature. NH_4OH was then added dropwise until the pH was 6.5. Then the solution was performed on a hotplate at 100 ℃ until a brown gel formed. Increasing the temperature to 300 ℃ to ignite the gel, large amounts of gas were given off and a lightweight voluminous powder formed rapidly. The resulting "precursor" power was

calcined at 1100 ℃ for 12 hours to form the hexa-ferrite phase.

Synthesis of RE ion doped Sr$_{1-x}$RE$_x$Fe$_{12}$O$_{19}$

The composition of the sample was taken according to reaction equation given
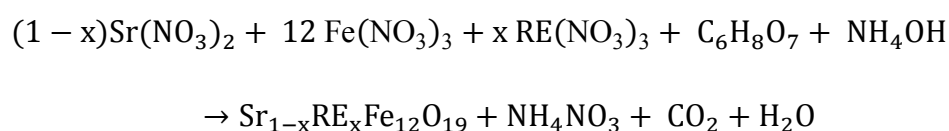
below:

$$(1 - x)Sr(NO_3)_2 + 12\,Fe(NO_3)_3 + x\,RE(NO_3)_3 + C_6H_8O_7 + NH_4OH$$

$$\rightarrow Sr_{1-x}RE_xFe_{12}O_{19} + NH_4NO_3 + CO_2 + H_2O$$

Table 3.2 Details of the chemical used in the synthesis for La doping

La content (x)	Weight of Sr(NO$_3$)$_2$/g	Weight of La(NO$_3$)$_3$ · 9H$_2$O/g	Weight of Fe(NO$_3$)$_3$ · 9H$_2$O/g	Weight of Citric acid/g
0	0.1284	0	2.7876	1.5750
0.1	0.1156	0.0260	2.7876	1.5750
0.15	0.1091	0.0390	2.7876	1.5750
0.2	0.1027	0.0520	2.7876	1.5750
0.25	0.0963	0.0650	2.7876	1.5750
0.3	0.0899	0.0779	2.7876	1.5750

Stoichiometric amounts of Sr(NO$_3$)$_2$, Fe(NO$_3$)$_3$ · 9H$_2$O and RE nitrate were

dissolved in a minimum amount of deionised water (100 ml for 0.1 mol of Fe3+) by

stirring on a hotplate at 60 ℃. Citric acid was dissolved into the solutions to give a

molar ratio of metal ions to citric acid of 1:1. Table 3.1 shows the weight details of

the chemical used. Then the solutions were allowed several minutes to cool down to

room temperature. NH$_4$OH was then added dropwise until the pH was 6.5. Then the

solution was performed on a hotplate at 100 ℃ until a brown gel formed. Increasing

the temperature to 300 ℃ to ignite the gel, large amounts of gas were given off and a

lightweight voluminous powder formed rapidly. The resulting "precursor" power was calcined at 1100 ℃ for 12 hours to form the hexa-ferrite phase.

3.3 Sample Characterization

3.3.1 X-ray Diffraction (XRD)

Bruker D8 Advanced X-ray diffractometer with Cu-Kα radiation (wavelength λ=1.54056 Å) was used to find the crystallinity and phase of samples. The samples were prepared by spreading nanoparticles on a zero background (Si) sample holder. Diffraction pattern was obtained at room temperature between $20 - 75^o\,2\theta$ angles. The patterns were matched with ICCD database.

Scherrer's equation was used to calculate the size of particles from the full width at half maximum for the diffraction peaks. The Scherrer's equation is given [23],

$$D = 0.9\lambda/\beta Cos\theta \qquad\qquad (3)$$

Where "D" is the average particle size, "λ" is the wave length of X-rays (0.15406 nm), "θ" is the Bragg's angle, and "β" is the value at full width half maxima (FWHM, additional broadening in radians).

3.3.2 Transmission Electron Microscope (TEM)

JEOL's JEM1200EX II TEM was used to study the particle size of Strontium hexagonal ferrites. This TEM uses an accelerating voltage of 120 kV and can reach a magnification up to X 500K times. TEM samples were prepared by dropping a drop

of ultrasonicated aqueous Al and RE doped Strontium hexagonal ferrite samples on carbon coated copper grid.

3.3.3 Differential Scanning Calorimeter (DSC)

DSC studies are used to find the transition temperature of samples at exothermic and endothermic reactions. The studies have been carried out with TPI - 910 Cell Base. The DSC was performed between 25 ^{o}C to 600 ^{o}C at the heating rate of 10 ^{o}C/min. The study of DSC gives the idea how the sample absorbs or evolves heat during phase transitions, the enthalpy of the sample can also be calculated by measuring the area under the transition peaks. We can get the curie temperature from the results.

3.3.4 Alternating Gradient Magnetometer (AGM)

The hysteresis loops of the samples were measured by AGM. From the results we can se the effects of substitution on the magnetic properties such as the saturation magnetization moment (Ms), coercive field (Hc), remenance (Mr).

3.3.5 Raman Spectroscopy

The Raman Spectroscopy was used to analyze accurately the vibrational spectra of Strontium hexagonal ferrites and Al, RE doped Strontium hexagonal ferrties to study their complex lattice dynamics of the five different Fe site. In 1997 J. Kreisel et. al. did the first Raman spectra study of barium hexaferrite [24]. They found the strongest Raman band at 684cm^{-1}, a characteristic peak of the M-hexaferrite

structure. The Raman spectroscopy study was performed at room temperature using

Enwave Raman spectroscopy using a red laser at 524nm.

Chapter 4 Results and Discussion

4.1 XRD Studies

$SrAl_xFe_{12-x}O_{19}$:

Fig. 4.1 shows XRD patterns taken after heating the combustion product ''precursor powder'' of Strontium ferrite ($SrFe_{12}O_{19}$, ICCD-080-1198) at different temperatures. It is easy to see the emergence of hexaferrite phase at around 800 ℃. The pure phase hexaferrite is obtained at 1100 ℃.
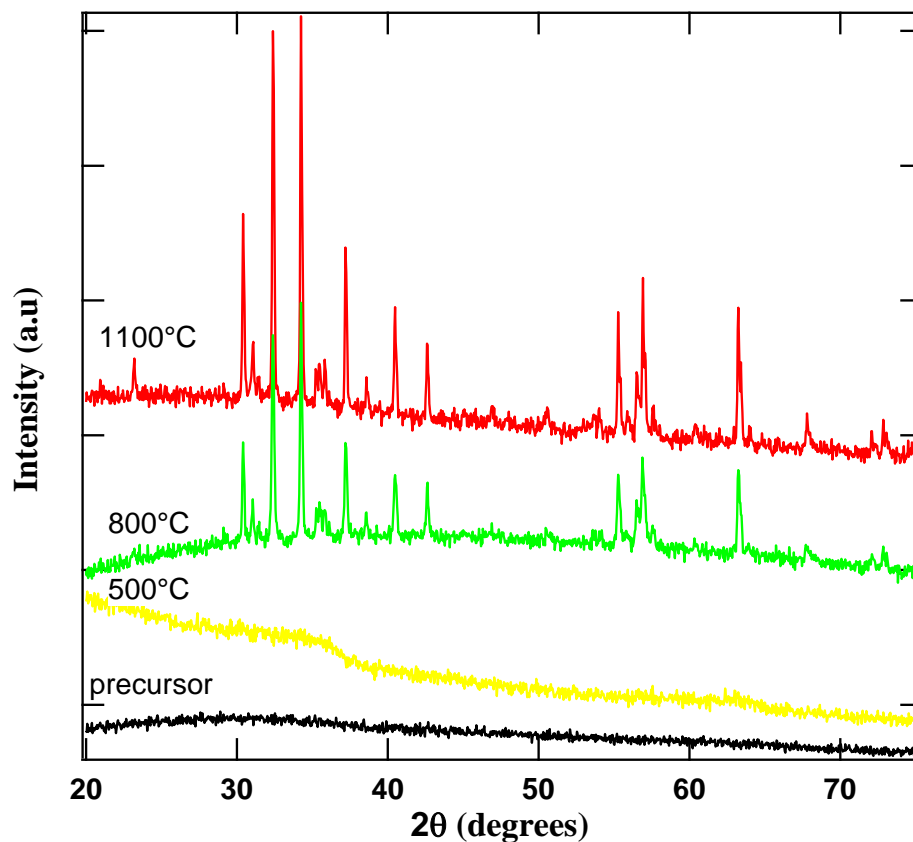
Fig. 4.1 XRD patterns showing the phase evaluation of $SrFe_{12}O_{19}$ as a function of temperature.

X-ray diffraction patterns for $SrFe_{12}O_{19}$ is plotted in Fig. 4.2. The crystal planes at different peaks were corresponds to pure phase hexaferrite without any formation of secondary phase. This result shows that pure hexaferrite can be synthesized using the sol-gel combustion method developed in this research. The crystallite size of $SrFe_{12}O_{19}$, as calculated using Scherrer's equation Eq. (3), was found to be 65 nm. The crystallite size was calculated from the full-width at half-maximum (FWHM) of the XRD reflection (107), (110), and (114) planes as shown in Fig.. 4.6.
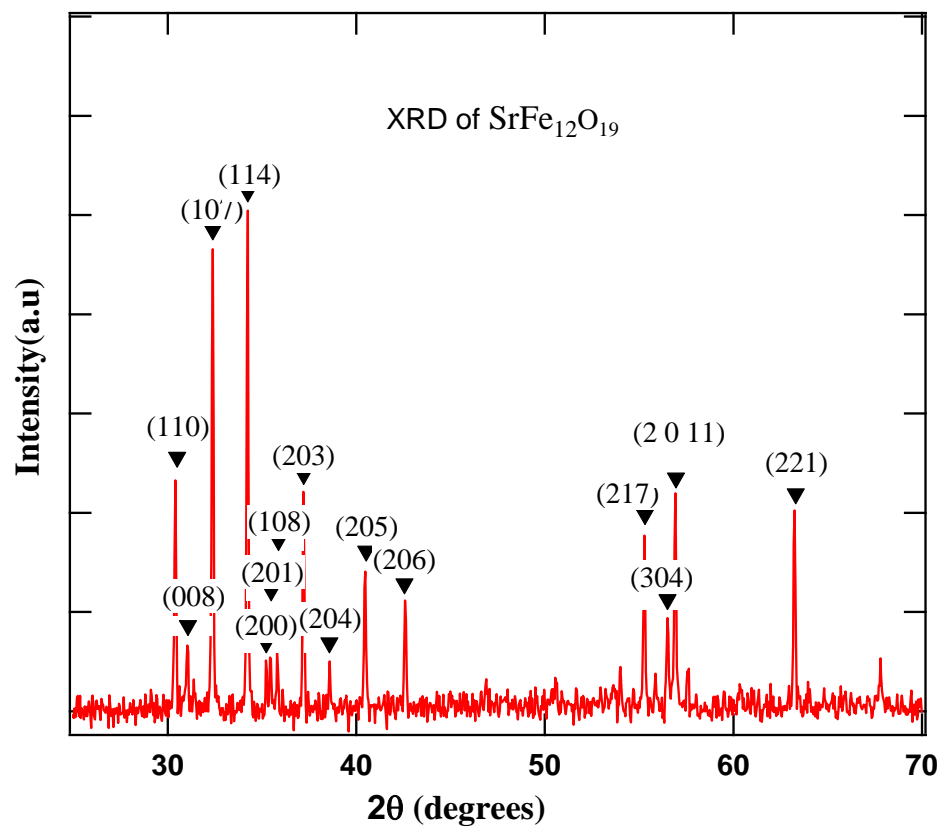
Fig. 4.2 XRD plot of $SrFe_{12}O_{19}$ sample calcined at 1100℃.

Fig. 4.3 shows the XRD patterns of different Al doped level $SrAl_xFe_{12-x}O_{19}$. From the Fig.ure we can see that with the Al doping level increasing, the peaks shift to the right. It is observed that Al doping does not affect the hexagonal crystal

structure of ferrite for high Al doping. The shift in XRD peaks to the right indicates
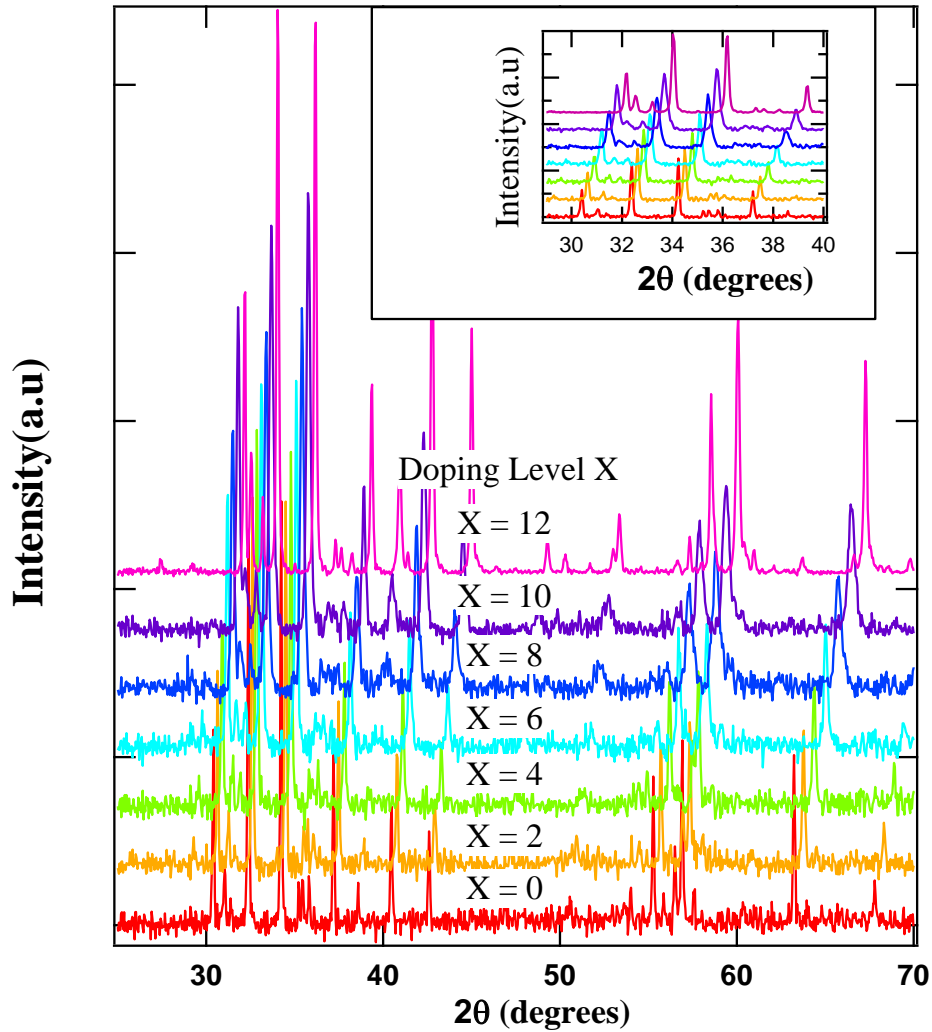
lattice contraction upon Al doping.

Fig. 4.3 XRD Patterns of $SrAl_xFe_{12-x}O_{19}$. The inset gives a close-up view.

An asymmetry in the intensity of peaks (107) and (110) $(\frac{I(107)}{I(110)})$ is observed in

Fig.. 4.4. It shows that the peak intensity ratio decreases up to (x = 6), then it starts to

increase. This predicts that the particle shape doesn't change much until x = 6. Then

the particles tend to grow in a preferred orientation (107) and leading to a plate-like or

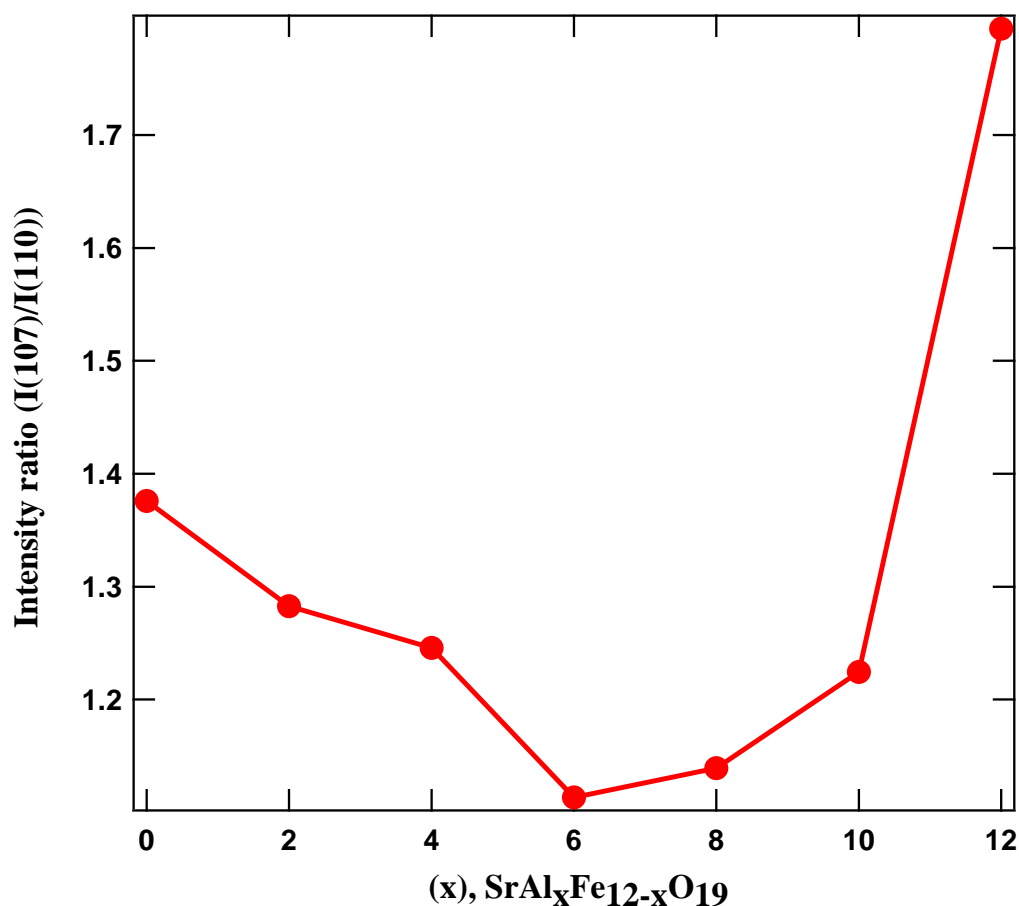rod-like morphology. The TEM images further confirm these results as discussed in section 4.2.

Fig. 4.4 Intensity ratio $\frac{I(107)}{I(110)}$ of $SrAl_xFe_{12-x}O_{19}$.

Fig. 4.5 is a comparison of theoretical doping levels and the measured doping levels in individual particles measured using Energy Dispersive X-ray spectroscopy (EDX). It indicates that the Al composition of the materials formed was close to the theoretical calculation by the sol–gel combustion method. This shows samples are pure phase. It also shows that the applied method for $SrAl_xFe_{12-x}O_{19}$ synthesis produces single phase material.
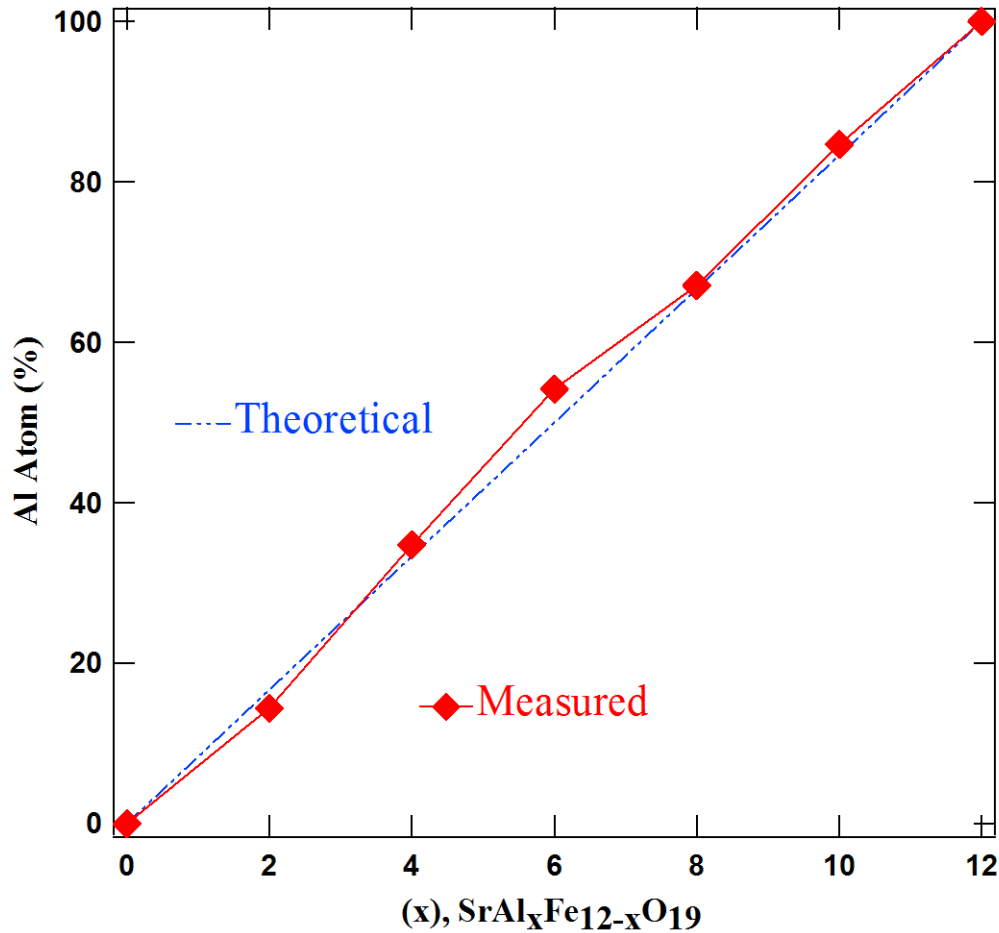
Fig. 4.5 Al% level n $SrAl_xFe_{12-x}O_{19}$ as measured using EDX.

Fig. 4.6 shows crystallite sizes of $SrAl_xFe_{12-x}O_{19}$ calculated using peaks at (110), (107), and (114). They are calculated using Scherrer's equation Eq.(2). With increasing the Al substitution, the FWHM of peaks corresponding to the (110), (107), and (114) directions increases up to x = 8 Al substitution. This indicates decrease in crystallite size with Al doping. This suggests that though the crystal structure does not change, the shape of the particles have varied. The crystallites will change from small spheres to large discs or needles with the Al substitution exceeding x = 8.
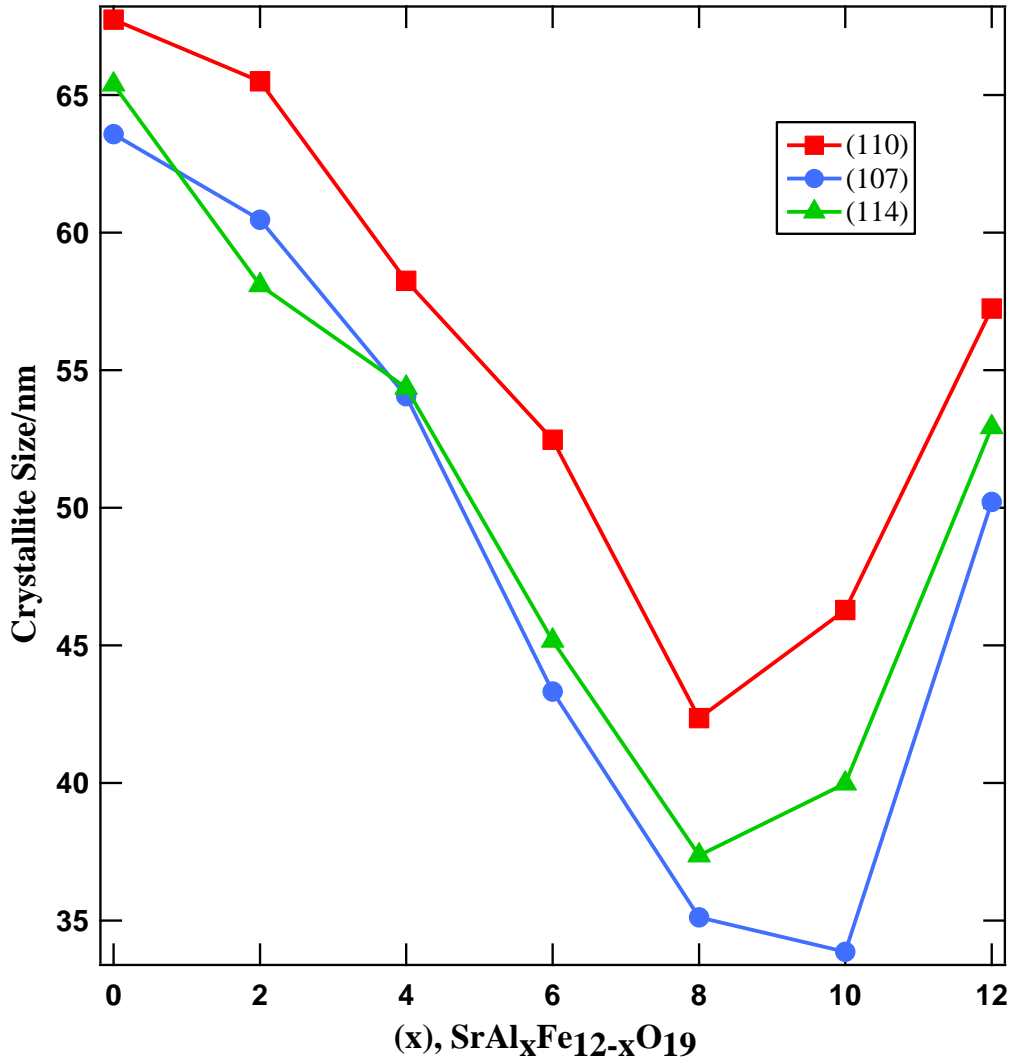
Fig. 4.6 Scherrer crystallite sizes of $SrAl_xFe_{12-x}O_{19}$.

Fig. 4.7 and Fig. 4.8 shows the lattice parameters for $SrFe_{12}O_{19}$. They were calculated by the following equation [21]:

$$d_{(hkl)} = \left(\frac{4}{3}\frac{h^2+hk+k^2}{a^2} + \frac{l^2}{c^2}\right)^{-\frac{1}{2}} \qquad (4)$$

This equation is used for calculating the hexagonal lattices parameters 'a' and 'c' [36]. It is evident from the Fig.ures that both lattice parameters decrease with the increase in Al content. This changes in lattice constant results from the difference in ionic radii of Al^{3+} ion (0.535 Å) and Fe^{3+} ion (0.645 Å) [28]. The smaller Al^{3+} ion, replacing

Fe^{3+} ion leads to lattice contraction of the unit cell. Overall, 5.4% and 3.9% lattice contraction is observed at x = 10 Al doping level as compared to the pure $SrFe_{12}O_{19}$.
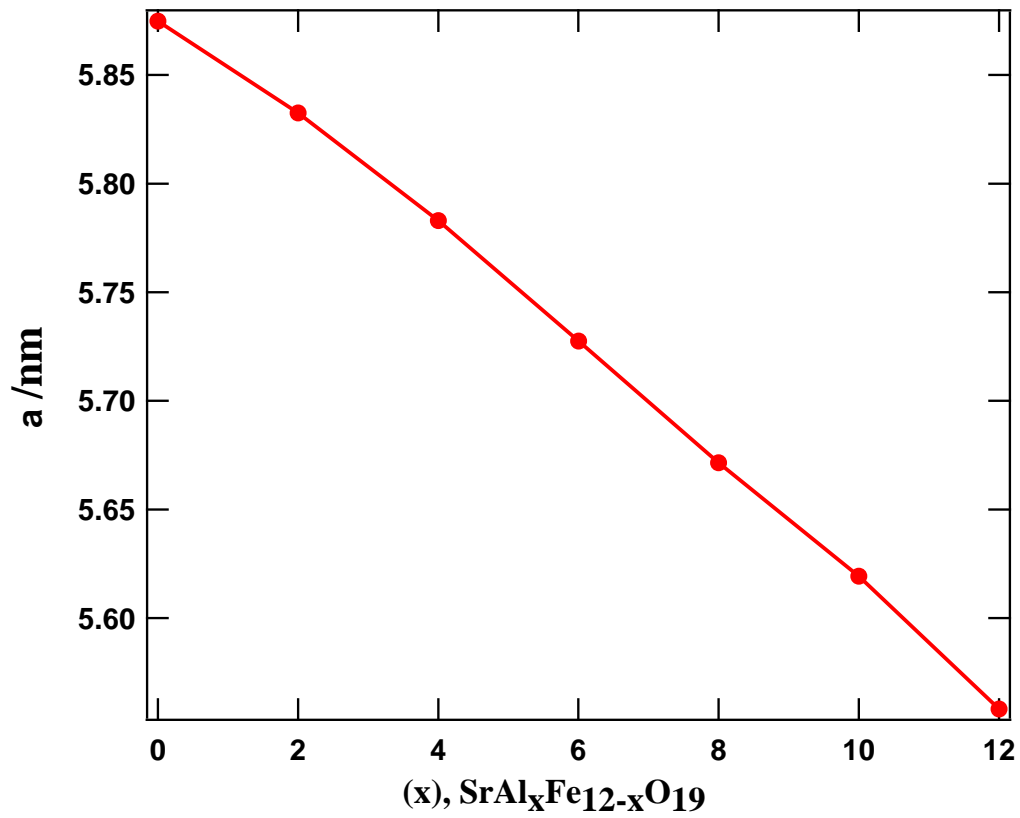
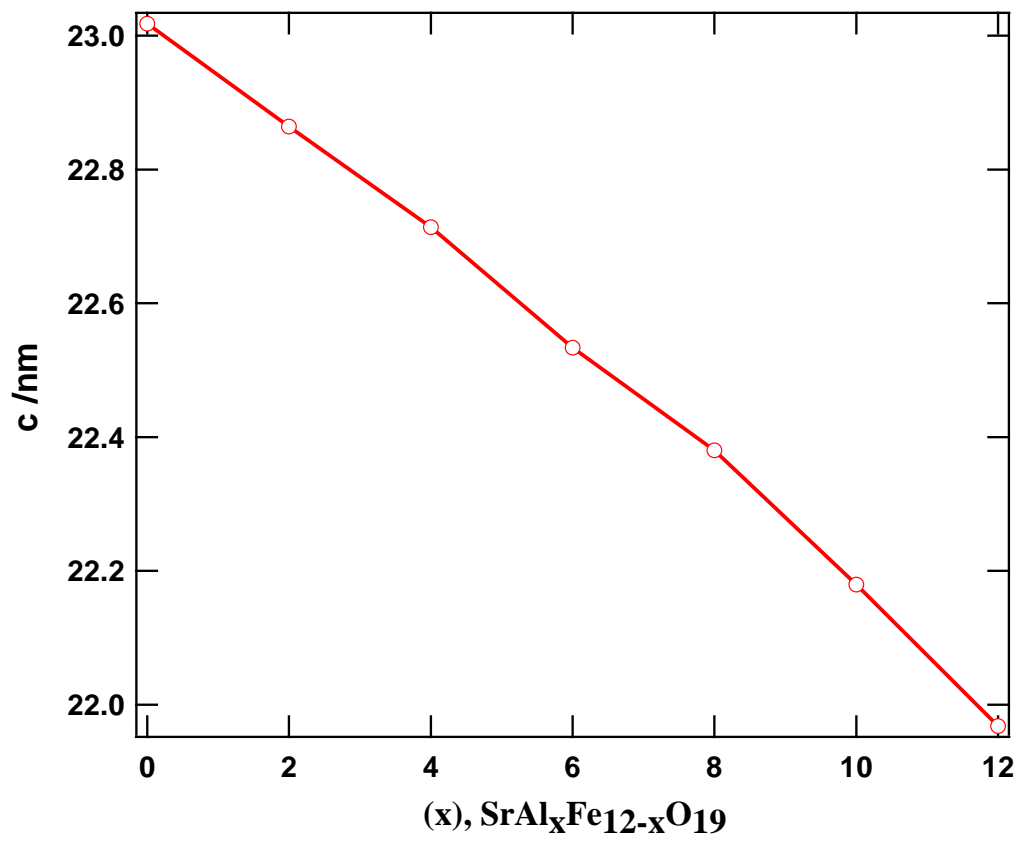

Fig. 4.7 Lattice constant 'a' of $SrAl_xFe_{12-x}O_{19}$.

Fig. 4.8 Lattice constant 'c' of $SrAl_xFe_{12-x}O_{19}$.

$Sr_{1-x}RE_xFe_{12}O_{19}$:

X-ray diffraction patterns for $Sr_{1-x}La_xFe_{12}O_{19}$ is plotted in Fig. 4.9. The XRD analyses reveal that, in all the patterns, the main peaks correspond to the hexagonal M-type phase. As compared to the Al substitution, the peaks don't shift to the right. It means that the lattice parameter of the samples does not change much, as shown in Fig. 4.10 and Fig. 4.11. However, as compared to $SrFe_{12}O_{19}$, the lattice parameter contracts. La ion (La^{3+} 1.17Å) is smaller than Sr ion (Sr^{2+} 1.32Å). The lattice parameter plots function show that the La substitution brings in more contraction along 'a' axis than along 'c' axis. This result is expected as La ion replaces Sr seating in based plane of the unit cell, in Fig. 1.2.
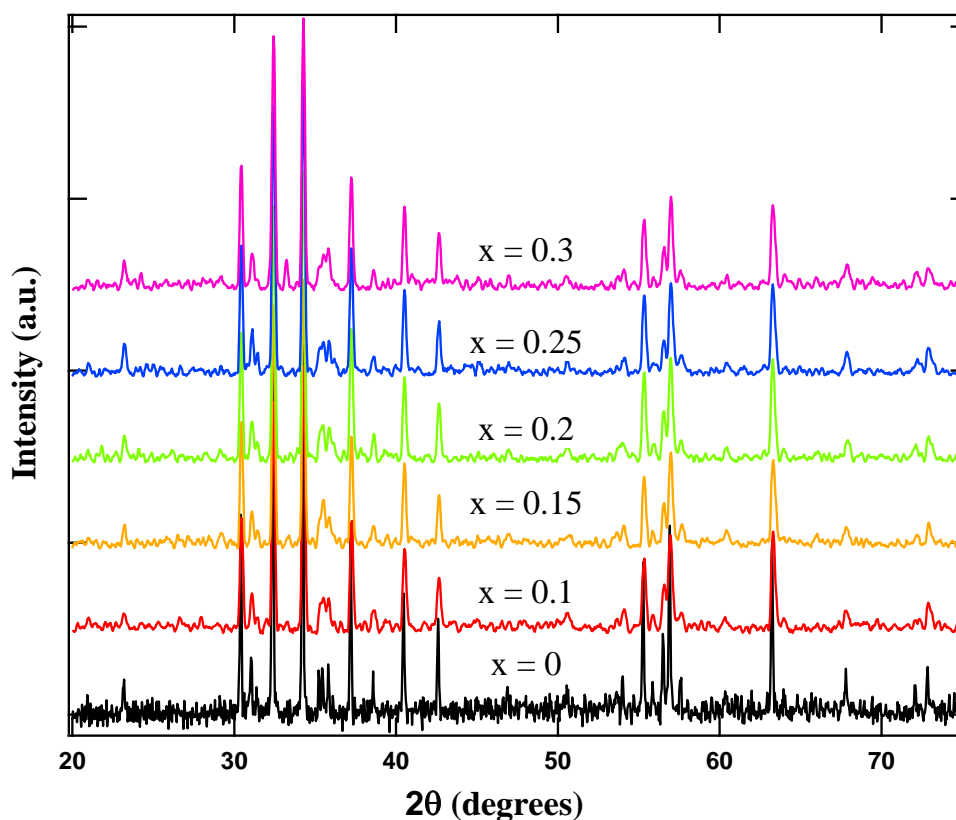

Fig. 4.9 XRD plot of $Sr_{1-x}LaFe_{12}O_{19}$ sample.

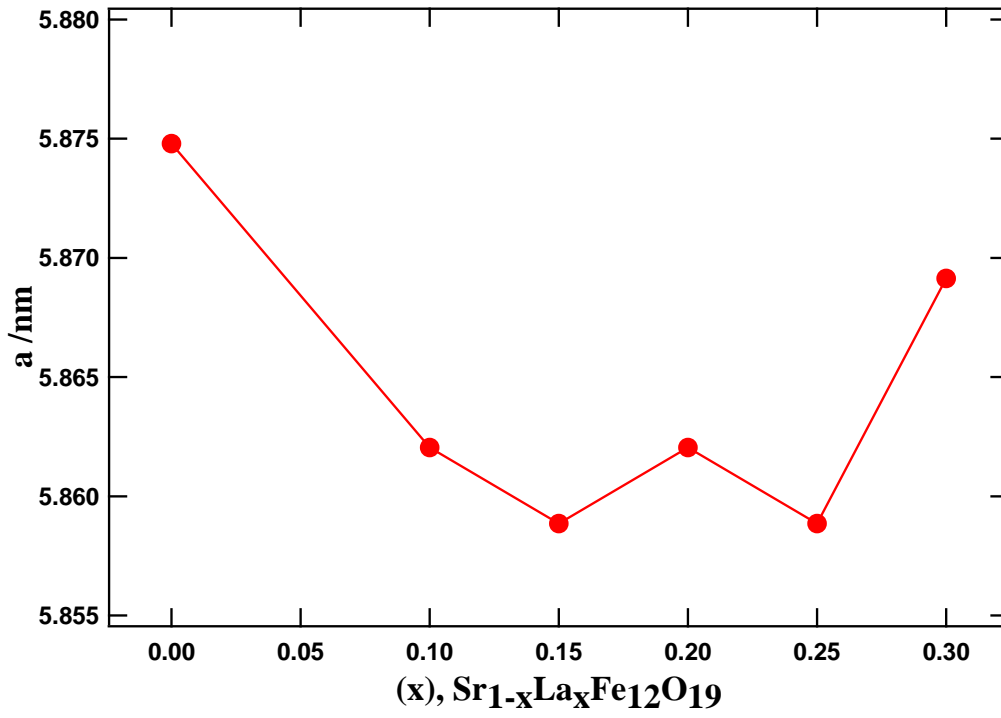Fig. 4.10 Lattice constant 'a' of $Sr_{1-x}La_xFe_{12}O_{19}$.
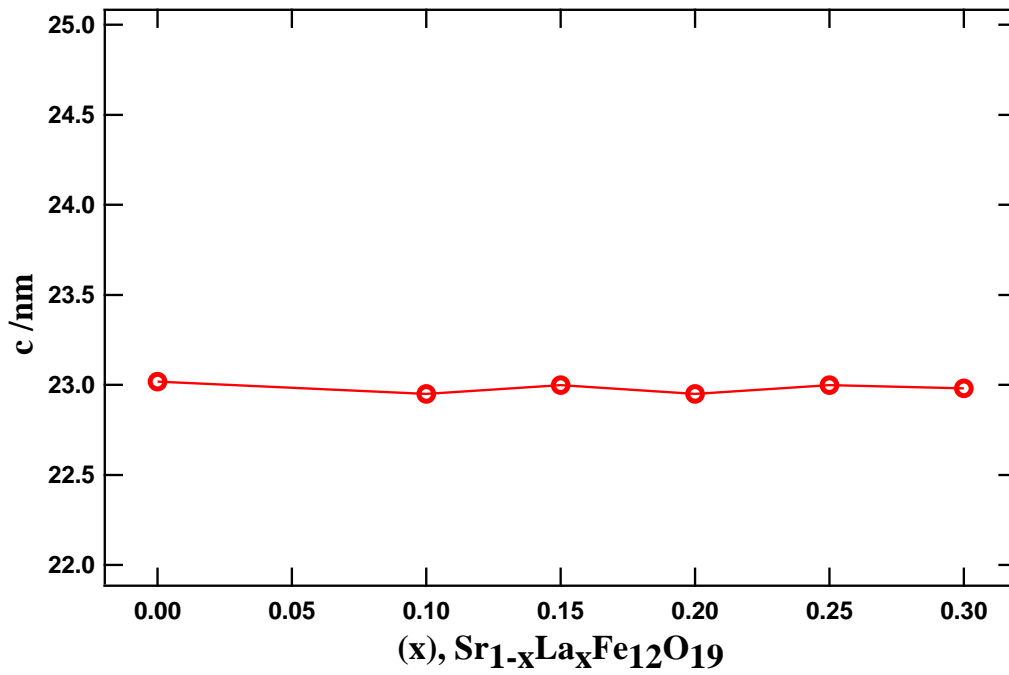
Fig. 4.11 Lattice constant 'c' of $Sr_{1-x}La_xFe_{12}O_{19}$.

$Sr_{0.9}RE_{0.1}Fe_{12}O_{19}$:

X-ray diffraction patterns for $Sr_{0.9}RE_{0.1}Fe_{12}O_{19}$ (RE = La, Sm, Gd) is plotted in Fig. 4.12. The XRD analyses reveal that, in all the patterns, the main peaks correspond to the hexagonal M-type phase. Compared to $SrFe_{12}O_{19}$, the peaks shift to a little right. The lattice parameters 'a' and 'c' as calculated using eq (4) is plotted in Fig. 4.13. The RE ion substitution does bring in lattice contraction along 'a' axis but the 'c' axis largely remains unaffected. Again the unit cell contraction can be explained on the basis of RE (RE = La, Sm, Gd) ions having smaller ionic radii La^{3+} 1.32Å, Sm^{3+} 1.098Å, Gd^{3+} 1.075Å, respectively, as compared to Sr^{2+} 1.32Å, and occupying the position in the unit cell.
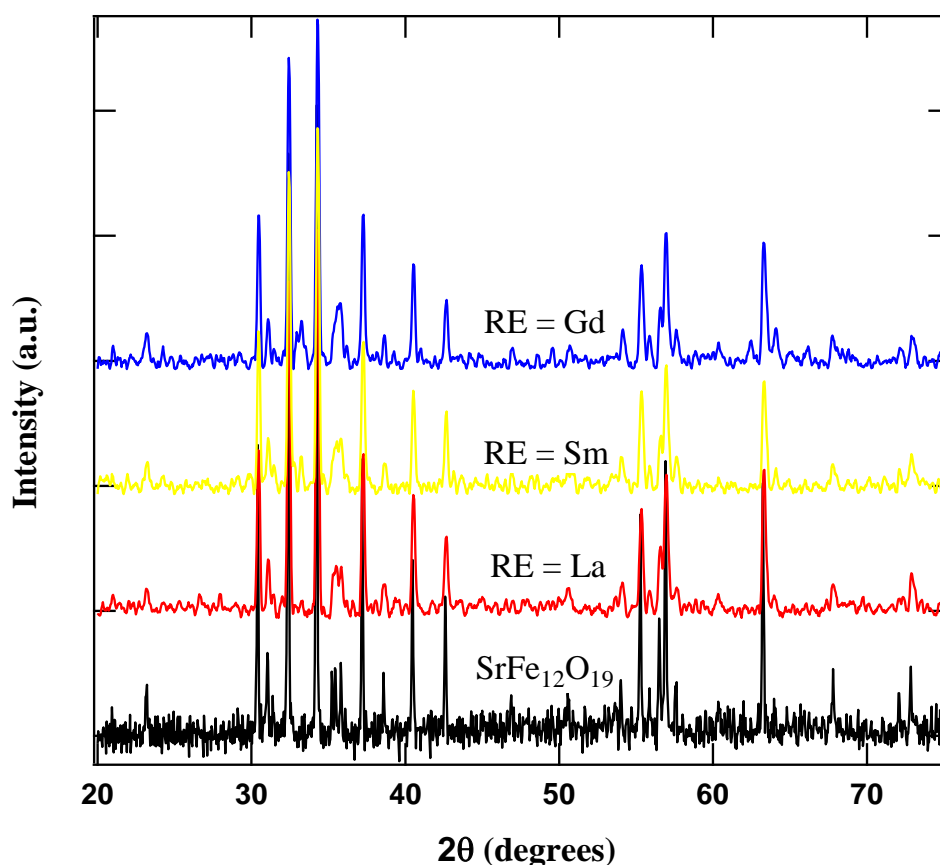

Fig. 4.12 XRD plot of RE ion doped $Sr_{0.9}RE_{0.1}Fe_{12}O_{19}$.
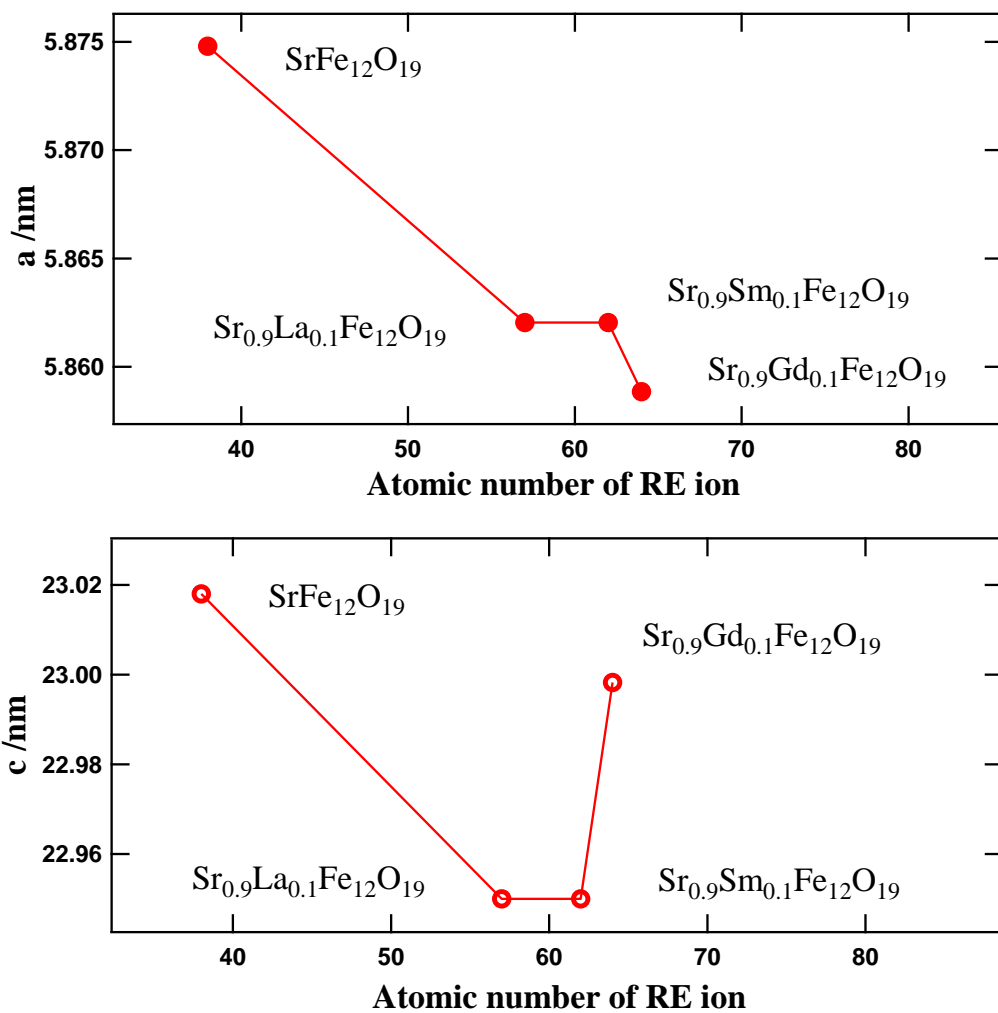
Fig. 4.13 Lattice constant 'a' and 'c' of RE ion doped $Sr_{0.9}RE_{0.1}Fe_{12}O_{19}$ as a function of RE ion atomic number.

4.2 TEM Studies

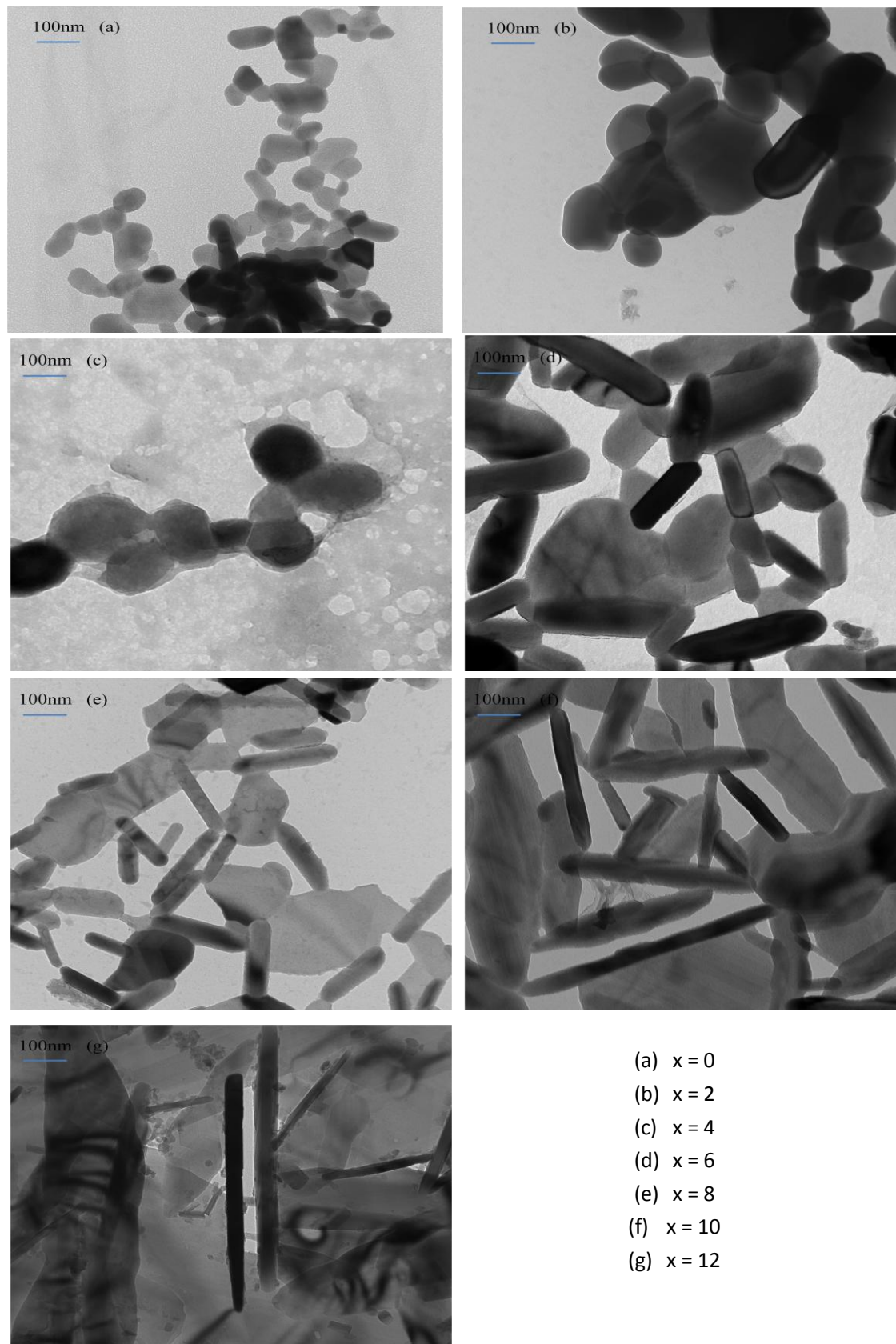Fig. 4.14 Transmission electron micrographs of $SrAl_xFe_{12-x}O_{19}$.

(a) x = 0
(b) x = 2
(c) x = 4
(d) x = 6
(e) x = 8
(f) x = 10
(g) x = 12

TEM images Fig. 4.14 describe the size variation of $SrAl_xFe_{12-x}O_{19}$. They show nanoparticles change size and morphology with increasing Al doping level. Pure iron ferrite particles were hexagonal platelets [29]. Particles at low doping levels were irregular and angular like a rounded sphere. Up to the doping level of x = 6, the particles lengthened, becoming like rods. At the doping level x = 12 the length of the particles reach 800 nm. Aspect ratio of nanoparticles is given by the ratio of length to width of the particles. Variation in aspect ratio of these particles with Al doping is plotted in Fig. 4.15.
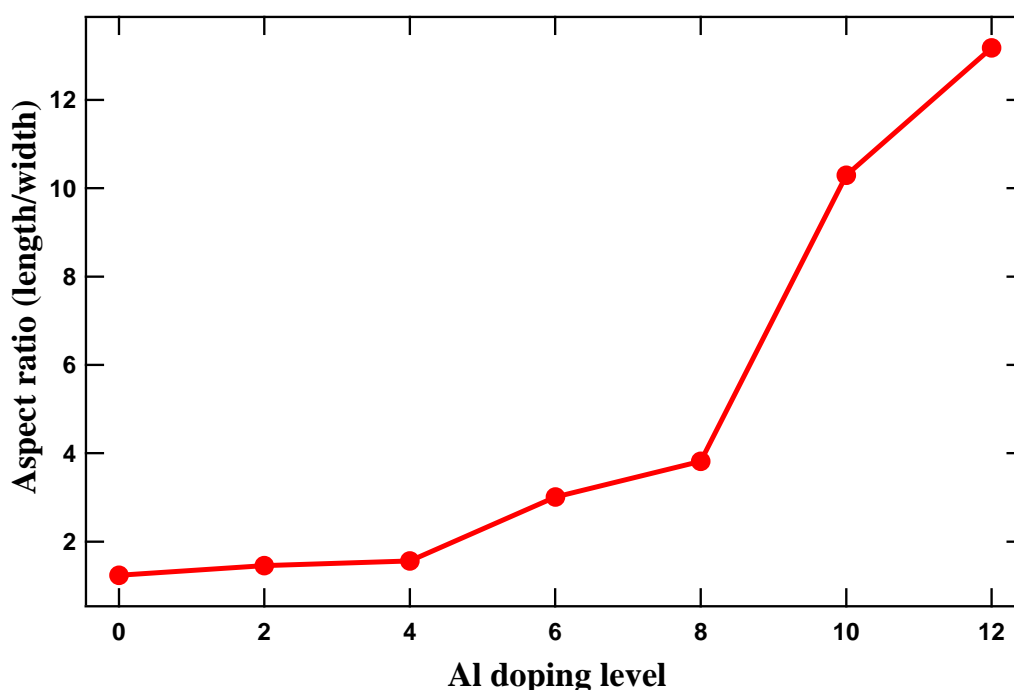

Fig. 4.15 Aspect ratio of $SrAl_xFe_{12-x}O_{19}$.

From Fig. 4.15 it is clear that the aspect ratio does not change too much up to x = 6. This result is in confirmation the XRD results. Above x = 8 Al doping, the morphology of the particles changes from small spheres to needles.

A representative TEM images of $Sr_{0.9}La_{0.1}Fe_{12}O_{19}$ synthesized by the combustion sol-gel method is shown in Fig. 4.16. When compared to the TEM images of $SrFe_{12}O_{19}$ in Fig. 4.15, the particle shape of RE ion doped $SrFe_{12}O_{19}$ is very similar.
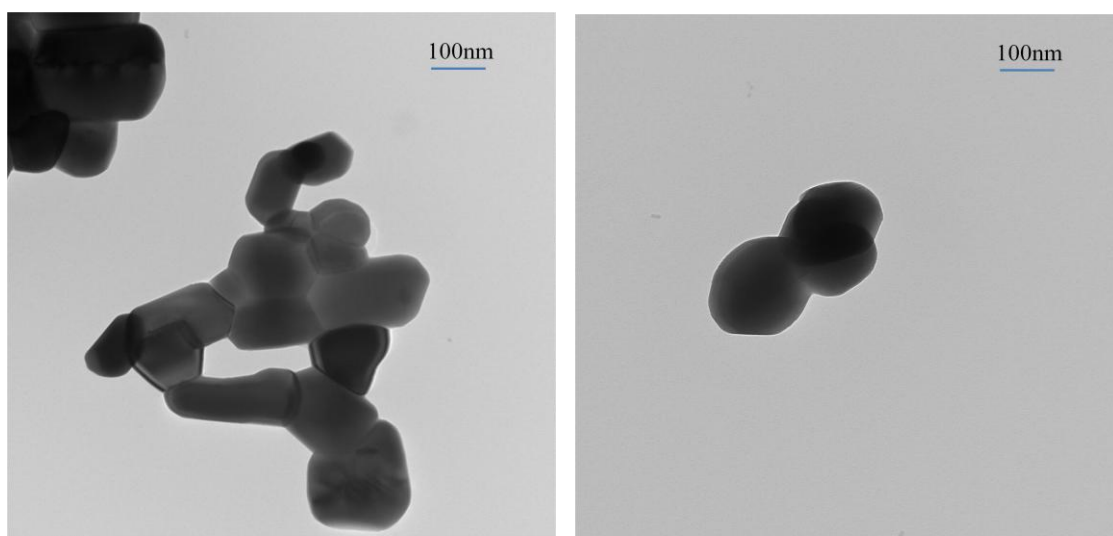

Fig. 4.16 Transmission electron micrographs of $Sr_{0.9}La_{0.1}Fe_{12}O_{19}$.

4.3 Thermal Characterization

Differential Scanning Calorimetric (DSC) is performed to study the phase transition temperatures in ferrites.
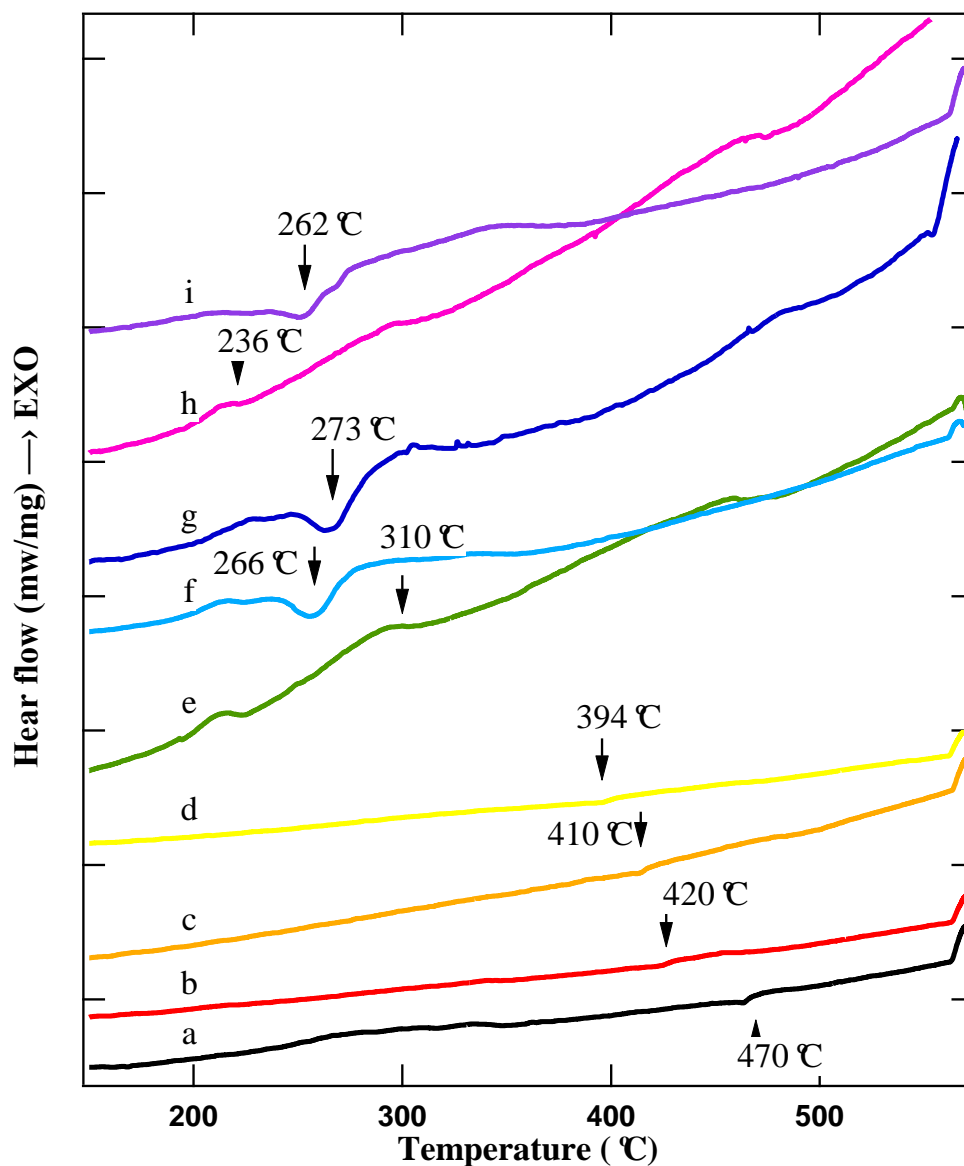
Fig. 4.17 DSC plot of $SrAl_xFe_{12-x}O_{19}$, (a) x = 0, (b) x = 0.5, (c) x = 1, (d) x= 1.5, (e) x = 2, (f) x = 6, (g) x= 8, (h) x = 10 and, (i) x = 12.

An endothermic peak at around 470℃ is observed for pure $SrFe_{12}O_{19}$. This endothermic peak corresponds to the Curie temperature, a temperature corresponding

to ferromagnetic to paramagnetic transition of the pure $SrFe_{12}O_{19}$. This result is in agreement with the published literature value [35]. Fig. 4.17 shows that up to the substitution level of x = 6, the Tc decreases with increasing Al doping level. When the substitution level increases over 6, the Tc nearly remains the same around 270℃. Table 4.1 lists the values of Tc for $SrAl_xFe_{12-x}O_{19}$.

Table 4.1 Curie temperature of $SrAl_xFe_{12-x}O_{19}$

x	0	0.5	1	1.5	2	6	8	10	12
Tc/℃	470	420	410	394	310	266	273	236	262

The observed change in Tc value is related to the super-exchange interaction between Fe^{3+} at 12k sites and 2b sites. Superexchange is a result of the electrons' having come from the same donor atom and being coupled with the receiving ions' spins. If the two next-to-nearest neighbor positive ions are connected at 90 degrees to the bridging non-magnetic anion, then the interaction can be a ferromagnetic interaction. Curie temperature is dependent on the super-exchange interaction between iron atoms. Higher the exchange energy, higher is the Tc value. For example with Fe super-exchange energy is changed by doping admixture ions (Co^{2+} and Zr^{4+}) [37], Tc decreases. As we dope $SrFe_{12}O_{19}$, the crystal gets contracted, hence the strength of the exchange interaction decrease, which brings in change in the Curie temperature. According to our observation, Al atoms are suppose to occupy 12k sites and 2b sites replacing iron atoms. When Al^{3+} ions replace the Fe^{3+} ions, the super-exchange interaction between $Fe^{3+} - O - Fe^{3+}$ decreases. The gradual

replacement of Fe by Al, reduces over all super-exchange interaction between 12k sites & 2b sites resulting in lowering of Tc value.

From Fig. 4.18 it is observed that Tc doesn't change much with the RE ion substitution. The Curie temperature is largely determined by the inter-atomic exchange interaction between iron ions (Fe^{+3}-O-Fe^{+3}). At this RE doping level, the RE atoms mainly replace the Sr atom, which would not affect the Fe^{+3}-O-Fe^{+3} exchange interaction too much, so the Curie temperature Tc are nearly the same.

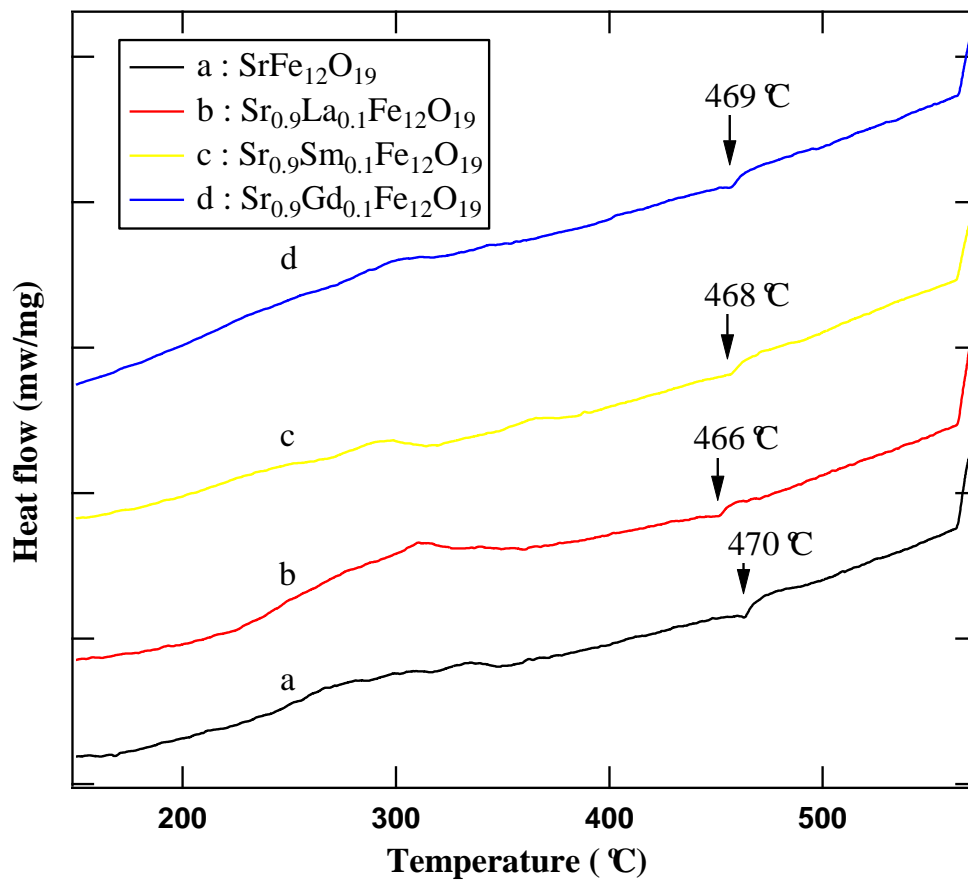Fig. 4.18 DSC plot of $SrFe_{12}O_{19}$ and $Sr_{0.9}RE_{0.1}Fe_{12}O_{19}$.

4.4 Magnetic Studies

4.4.1 Sample Preparation:

In order to minimize the demagnetization factor correction, the samples were embedded in epoxy and were aligned under 10 kOe field.

Fig. 4.19 The sample used for AGM measurements.

To understand the magnetization process, the hysteresis loop at RT were measured for $SrFe_{12}O_{19}$, $SrAl_2Fe_{10}O_{19}$, for $SrAl_xFe_{12-x}O_{19}$ (x = 4,6,8,10,12) and $Sr_{1-x}RE_xFe_{12}O_{19}$ (RE = La, Sm, Gd).

4.4.2 Results

The magnetization loops of samples as a function of applied field at room temperature are shown in Fig. 4.20 and Fig. 4.21 for Al doped $SrAl_xFe_{12-x}O_{19}$. The pure $SrFe_{12}O_{19}$ shows saturation magnetization of 59.76 emu/g and coercivity of 4.3 kOe. This high value of saturation magnetization and coercivity, as compared to previous results by Huang et al [39], show the high purity of our samples.
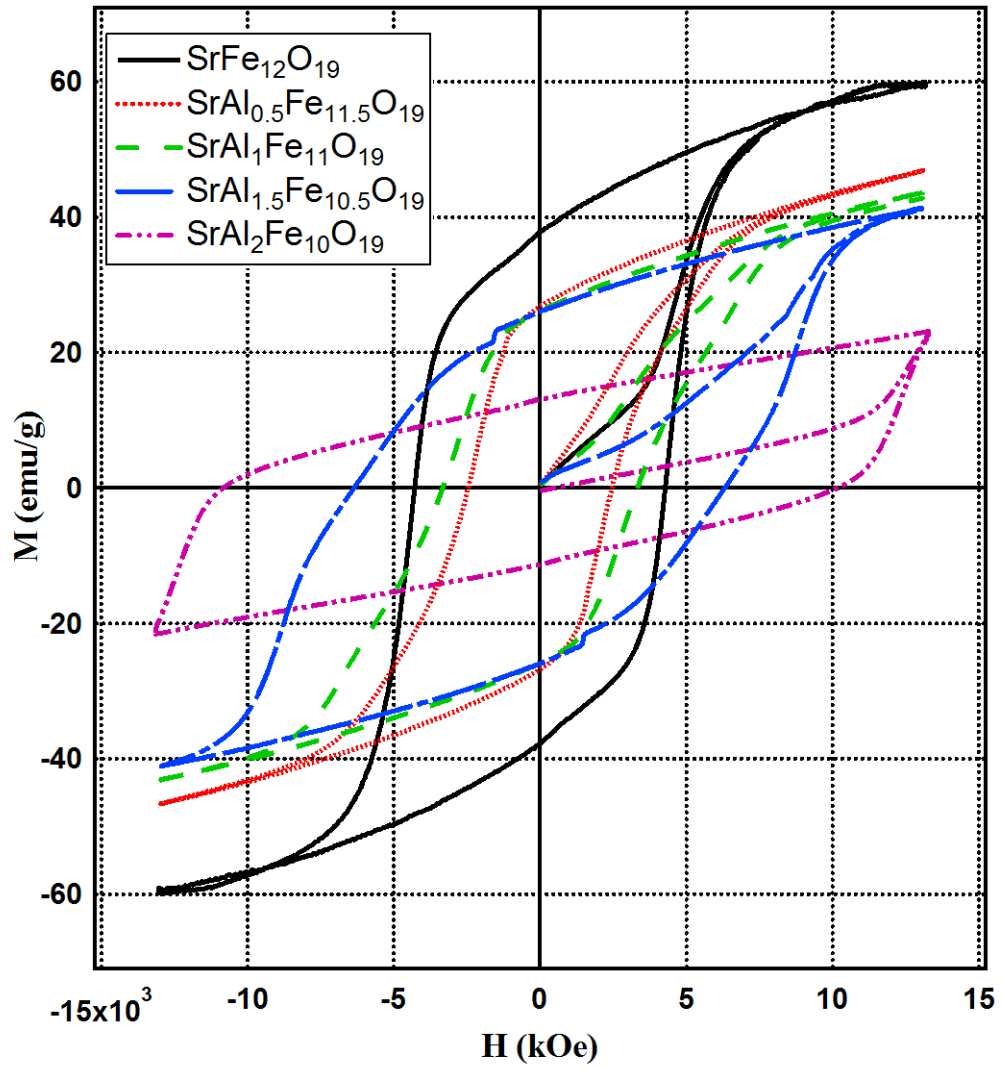
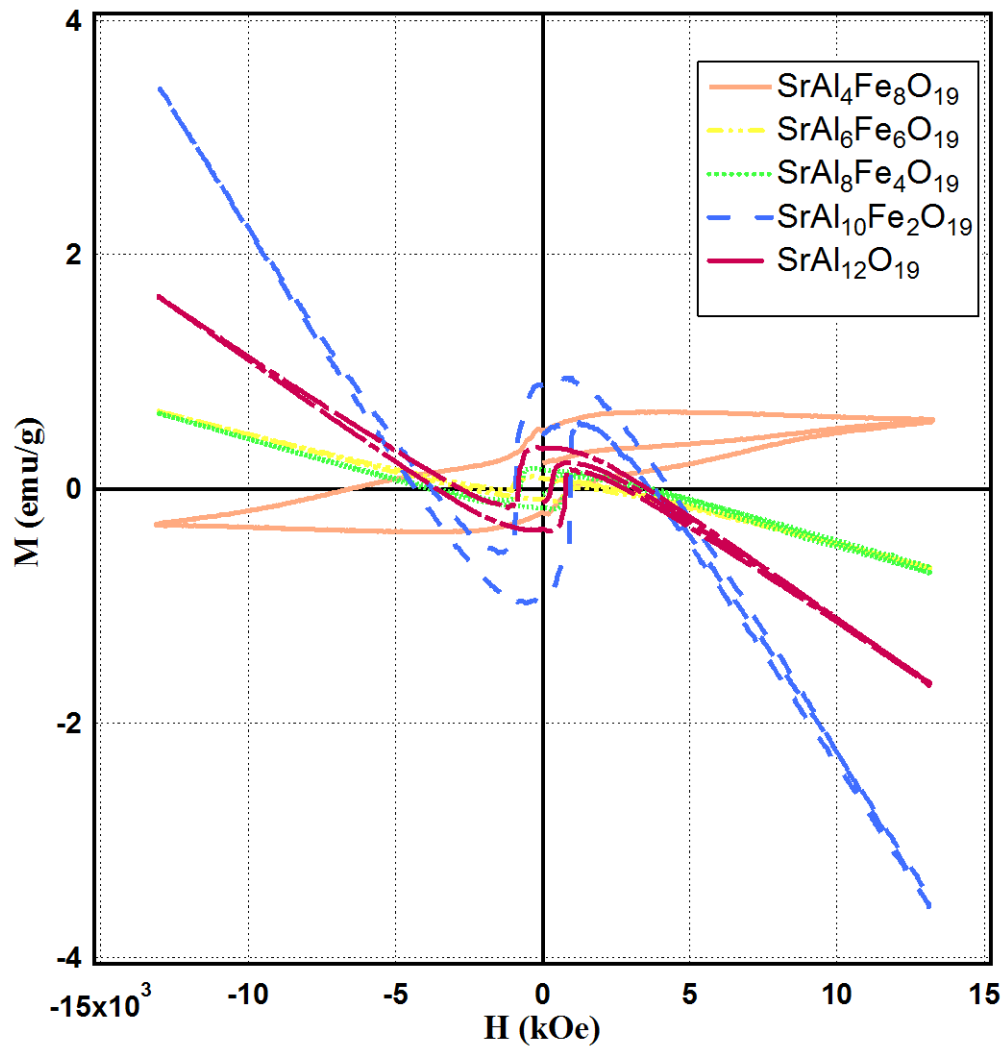Fig. 4.20 M vs. H hysteresis loops of $SrFe_{12}O_{19}$ to $SrAl_2Fe_{10}O_{19}$.

Fig. 4.21 M vs. H hysteresis loops of the series of samples Al doped $SrAl_xFe_{12-x}O_{19}$.
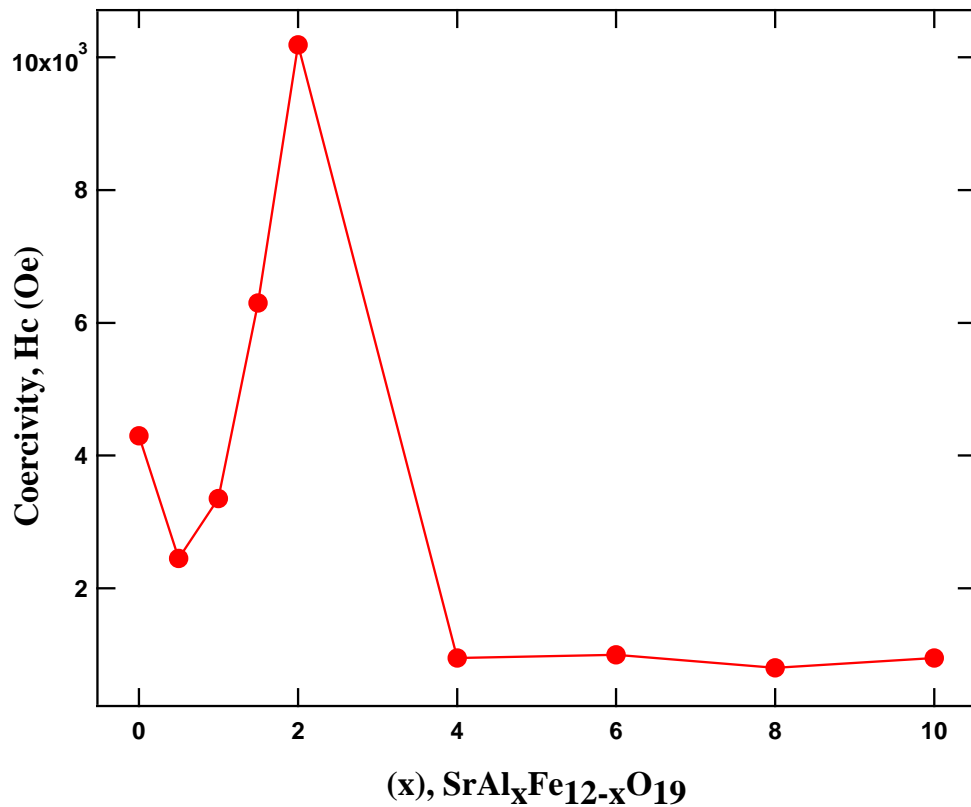
Fig. 4.22 Coercivity of $SrAl_xFe_{12-x}O_{19.}$

From Fig. 4.20, it is observed that low level of Al doping, up to x = 2, decreases the magnetization but brings in enhancement in the coercivity. The coercivity plotted as a function of Al substitution. Fig. 4.22 shows a five-fold increase in the coercivity at x =2 Al substitution, from the values of 4.30 kOe to 10.19 kOe for x = 0 to x = 2, respectively. At higher Al substitution, x > 2 level, the Hc value decreases to 0.95 kOe. The magnetization (***Ms***) decreases rapidly from 59 emu/g to 0.59 emu/g for x = 2 to x = 4, respectively. Liu et. al. [30] also obseved increase in coercivity up to x = 2 to a value of 7.7 kOe, and decrease in Ms above x = 2.

By increasing the Al component we observe the complexity of the magnetic phases which leads to the loop patterns as shown in Fig. 4.15. The Al doped Strontium hexagonal ferrite changes from ferromagnetic materials to ferrimagnetic materials as

the Al doping level increases. The expression for ferromagnetism of $SrFe_{12}O_{19}$ comes from the different sites of iron atoms located at 12k, 2b and 2a sites as shown in Table 1.3. When the Al atoms replace these iron atoms, the ferromagnetism decreases, so that the saturation magnetization decreases and the materials shows more ferrimagnetism. However, at last at x = 10, the Al atoms replace the iron atoms located at $4f_1$ and $4f_2$ sites. These iron atoms express ferrimagnetism. So the ferrimagnetism decreases a little finally. The saturation magnetization reduction with increasing Al^{3+} ion substitution can also be explained on the basis of the magnetic collinearity. For pure strontium ferrite, because of the existence of super-exchange interactions, the magnetic moments of Fe^{3+} ions are commonly arranged collinearity. With addition of the non-magnetic Al^{3+} ions into the iron sublattice, some super-exchange interactions will disappear, which causes the magnetic collinearity to break down, which results in *Ms* value reduction [30]. Thus, at higher Al concentration ferromagnetic is weakened. As these samples are at high external field, they behave as ferrimagnets due to the magnetization decreasing by the Al^{3+} replacing the Fe^{3+} at 12k and 2b sites, and the attracting negative value resulted from increased alignment of antiferromagnetic moments at $4f_1$ and $4f_2$ sites.

The $SrAl_xFe_{12-x}O_{19}$ coercivity is affected by two main factors, which are the particle size and substitution ion. Theoretically the coercivity will decrease with the particle size reduction. However, from the Stoner-Wolfforth model [31], the *Hc* value can be expressed as

$$Hc \propto \frac{K_1}{Ms}$$

Where K_1 is the magnetocrystalline anisotropy constant. When the substitution Al^{3+} content x is below 2, the *Ms* value decrease quickly, so the *Hc* value exhibits an increase. When the substituted Al^{3+} content is over 2.0, the coercivity will mainly be affected by the particle size, which is decreasing, so the *Hc* vale exhibits an decrease.
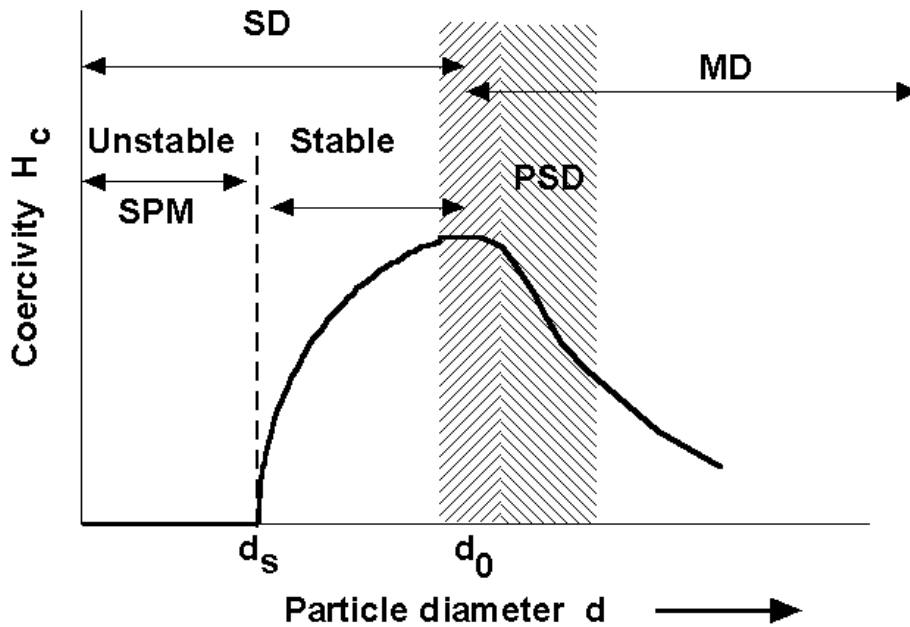

Fig. 4.23 Relation between coercivity and particle diameter.

Over the substitution level x = 4, the Ms decreases rapidly, the samples change from ferromagnetic to antiferromagnetic. It can be seen that when most Fe^{3+} ions are replaced by Al^{3+} ions, the particles still have the same coercivity. It may be the intrinsic coercivity of the O^{2-} ions.

From Fig. 4.24, one shows magnetization loops of $Sr_{1-x}Re_xFe_{12}O_{19}$ (RE = La) up to x= 0.3. As the La doping level increases, the saturation of the materails has a maximum value where the doping level is around x= 0.25. Thus, rare-earth substitution can enhance the magnetic properties of $SrFe_{12}O_{19}$. And Fig. 4.24 shows

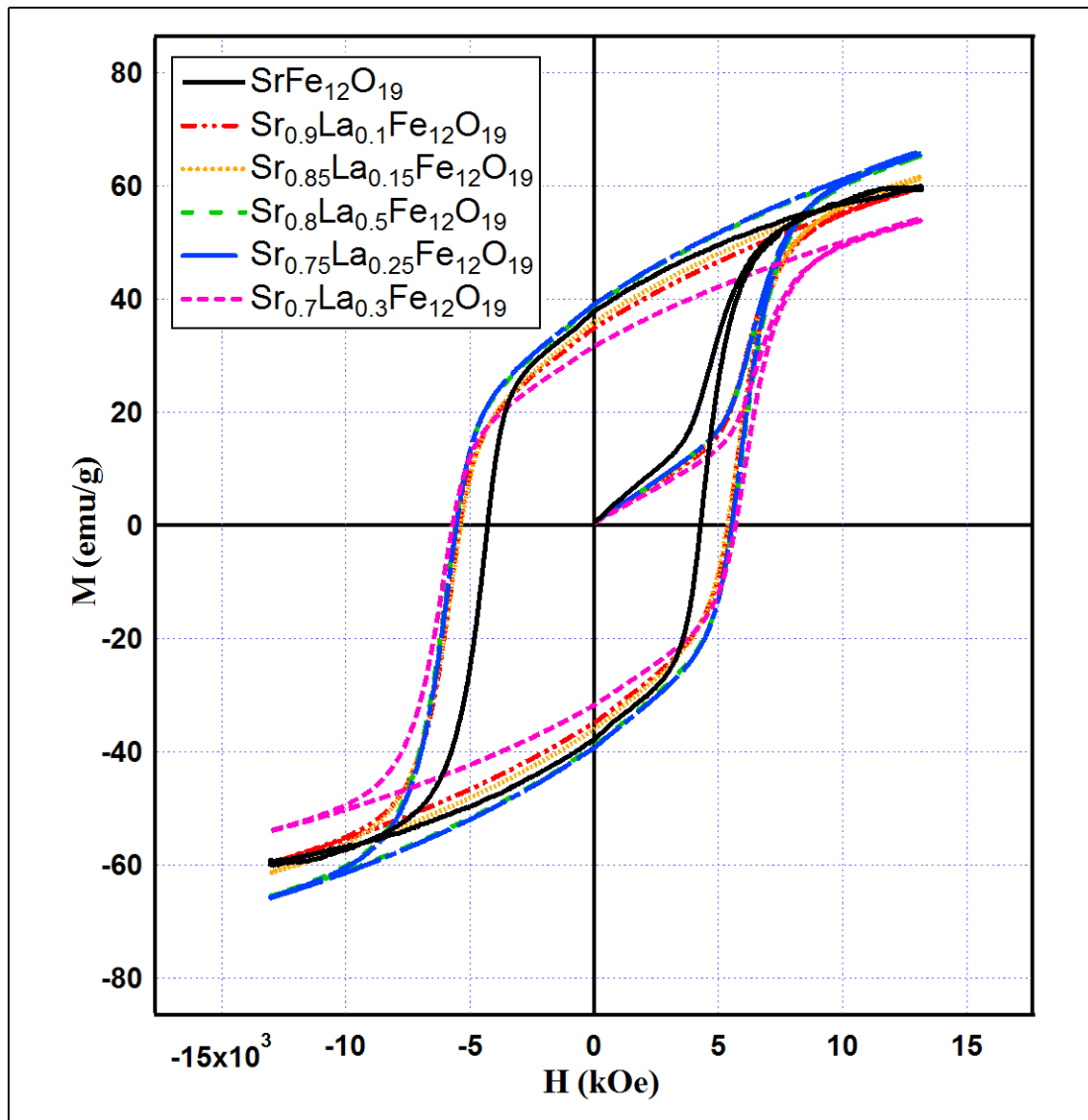the same results that around doping level x = 0.25 the materials can store the maximum energy.

Fig. 4.24 M vs. H hysteresis loops comparison of La doped $Sr_{1-x}La_xFe_{12}O_{19}$.

Table 4.2 Saturation Magnetization of $Sr_{1-x}La_xFe_{12}O_{19}$

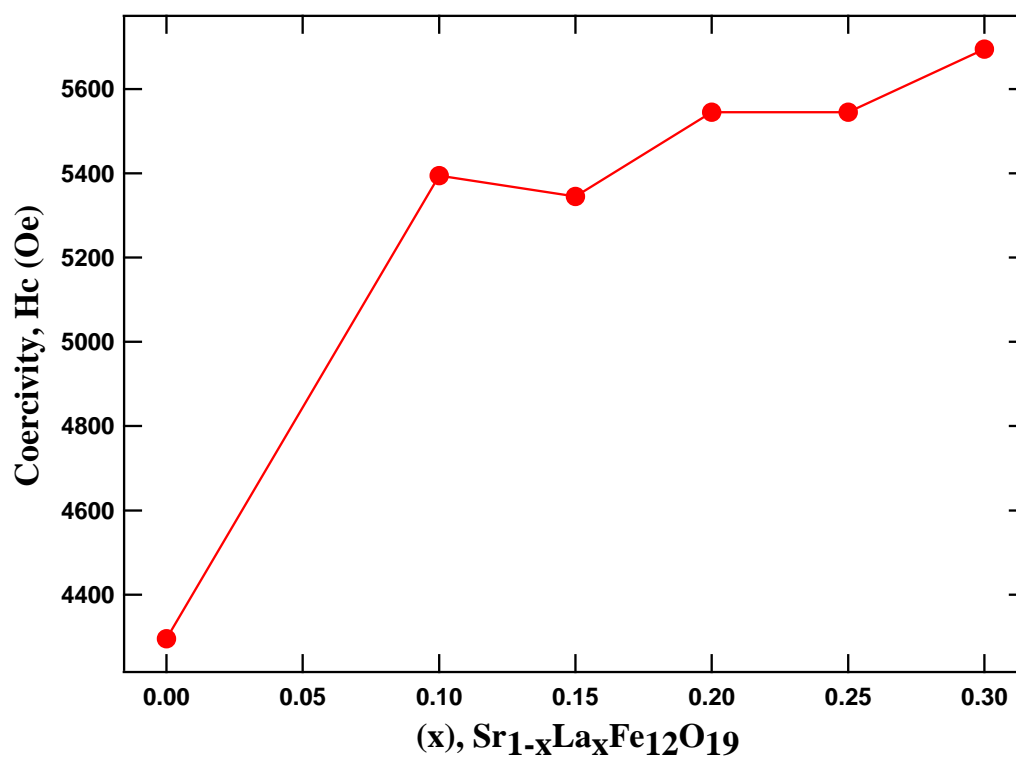| Type	Ms, (emu/g)	Type	Ms, (emu/g)
$SrFe_{12}O_{19}$	59.44	$Sr_{0.75}La_{0.25}Fe_{12}O_{19}$	65.59
$Sr_{0.9}La_{0.1}Fe_{12}O_{19}$	59.59	$Sr_{0.7}La_{0.3}Fe_{12}O_{19}$	53.83
$Sr_{0.85}La_{0.15}Fe_{12}O_{19}$	61.23	$Sr_{0.9}Sm_{0.1}Fe_{12}O_{19}$	56.55
$Sr_{0.8}La_{0.2}Fe_{12}O_{19}$	65.19	$Sr_{0.9}Gd_{0.1}Fe_{12}O_{19}$	56.33

Fig. 4.25 Coercivity of $Sr_{1-x}La_xFe_{12}O_{19}$ as a function of La doping.
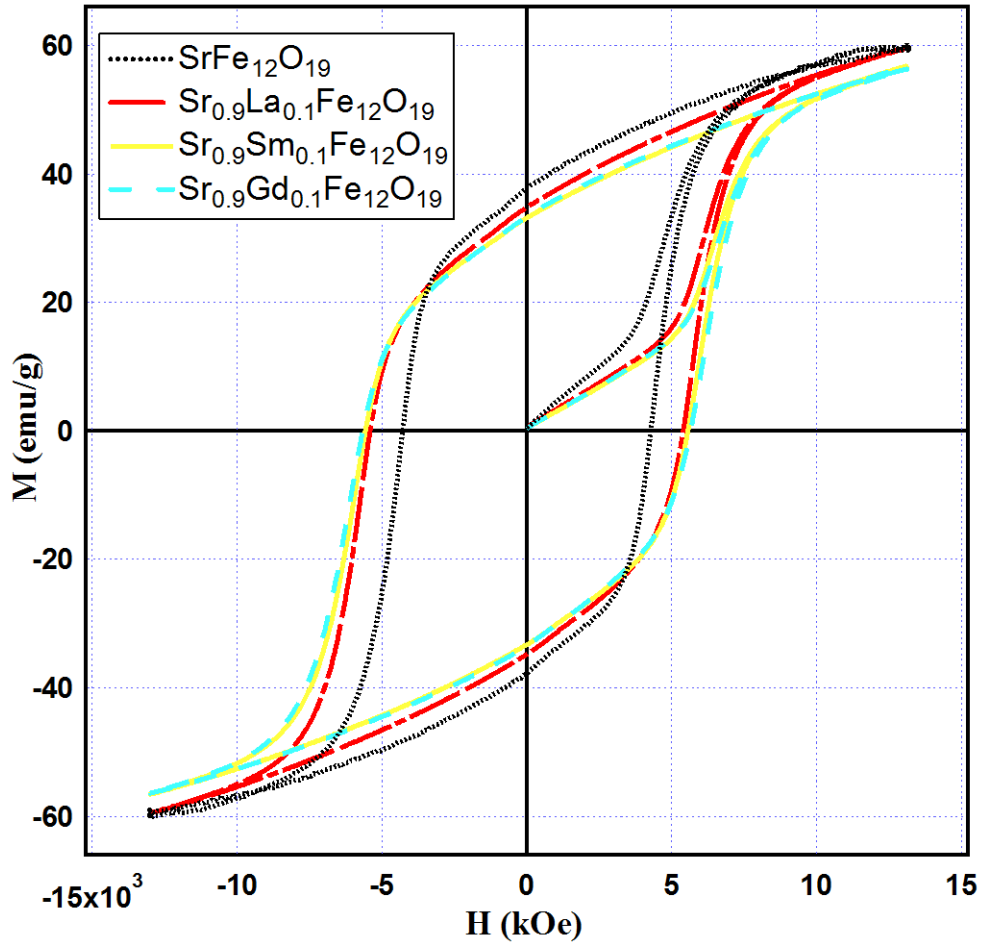
Fig. 4.26 M vs. H hysteresis loops comparison of the series of samples with rare-earth ion doped $Sr_{0.9}RE_{0.1}Fe_{12}O_{19}$.

Fig. 4.26 shows hysteresis loop at room temperature as a function of different RE doping (RE = La, Sm, Gd) in $Sr_{0.9}RE_{0.1}Fe_{12}O_{19}$. The saturation magnetization for $Sr_{0.9}RE_{0.1}Fe_{12}O_{19}$ is listed in the Table 4.2, As compared to La doping, $Sr_{0.9}RE_{0.1}Fe_{12}O_{19}$ shows comparatively lower saturation magnetization. The coercivity of RE ion doped $Sr_{0.9}RE_{0.1}Fe_{12}O_{19}$ samples is almost identical at a value of 5.1 kOe. However, an enhancement in coercivity upon RE doping is observed.

From Fig. 4. 24, Fig. 4.25 and Fig. 4.26, it can be seen that with the RE substitution, the coercivity of all the samples increase. In case of La doped sample H_c

increases because of the ionic anisotropy of La^{+3} ions has oblate in change distribution of 4f electrons. Although contraction of crystal and conversion of Fe^{+3} to Fe^{+2} decreases the exchange interaction but anisotropy due to anistropic charge distribution is sufficient to overcome those reduction hence H_c increases when doped with La^{+3} ions. Furthermore, the coercivity increases remarkably due to enhancement of the magnetic crystalline anisotropy [32] with anisotropic Fe^{2+} ions location on 2a site as usually found in rare-earth ion substitutions [33].

Overall, it is be observed the La substitution increases the saturation magnetizations Ms. The Ms reaches a maximum value x = 0.25 La substitution. The increase in Ms is attributed to enhancement of hyperfine fields at 12k and 2b sites as strengthening in the $Fe^{3+} - O - Fe^{3+}$ superexchange interaction giving higher net magnetization. After Ms reaches to a maximum value, the decreasing can be explained by two effects, 1) magnetic dilution with changing of the Fe^{3+} (high spin) valence state to Fe^{2+} (low spin) state on 2a site by substitution of the Sr^{2+} site with La^{3+} ions, and 2) existence of spin canting promoting reduction of superexchange fields [8, 34]. The $Fe^{3+} - O - Fe^{3+}$ superexchange interaction is disrupted and weakened by Fe^{2+} ions and canted spins, which would be produced by substitution of the La into the hexaferrites. These result in lower magnetization.

The hard magnets are characterized by the quantity called $(BH)_{max}$ energy product, which shows the strength of the magnet. Fig. 4.26 and Fig. 4.28 shows the energy product (BH) curves as a function of B. The maximum energy product $(BH)_{max}$ is the peak of the curve. Curves for different substitution level of La are

shown in Fig. 4.27. It appears that at x = 0.25 La doping, the sample has the maximum energy product.
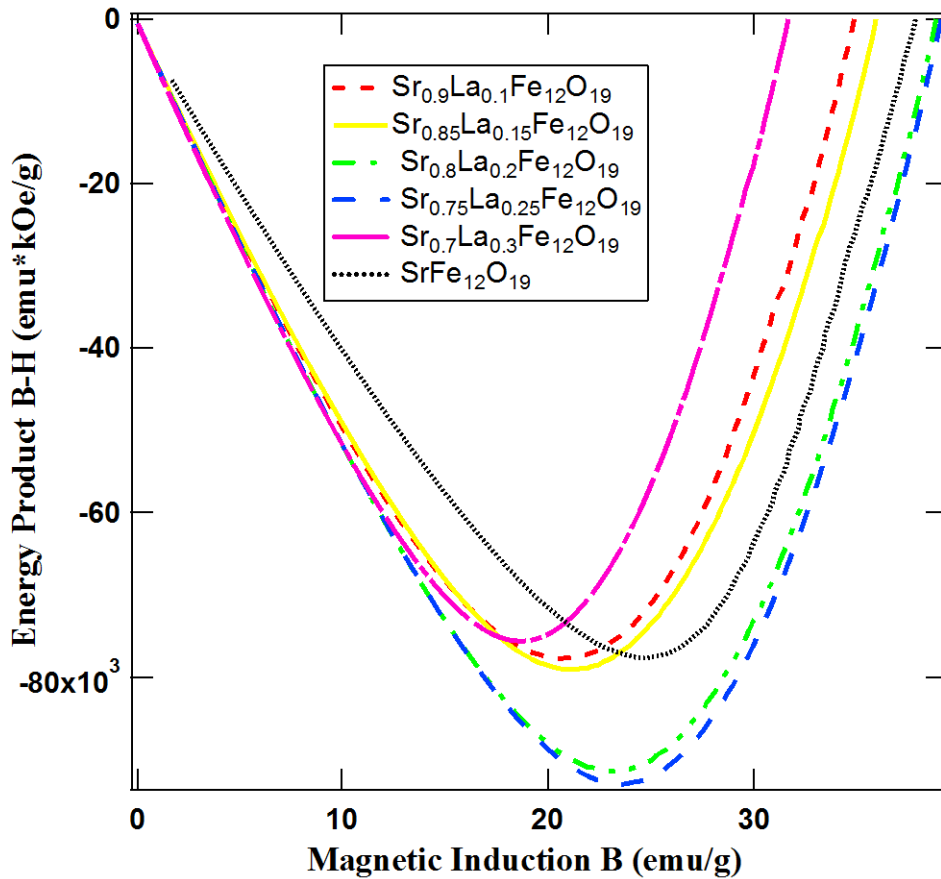
Fig. 4.27 Energy product vs magnetic induction 'B' of $Sr_{1-x}La_xFe_{12}O_{19}$.

Fig. 4.28 shows energy product (BH) curves as a function of 'B' for $Sr_{1-x}RE_xFe_{12}O_{19}$. It is observed that at the same substitution level, La doping brings in maximum energy product (BH) value at B = 21 (emu/g). All the RE doping will shift the peak of the curve to the left, which correspond that the RE doping can enhance the strength of the samples.
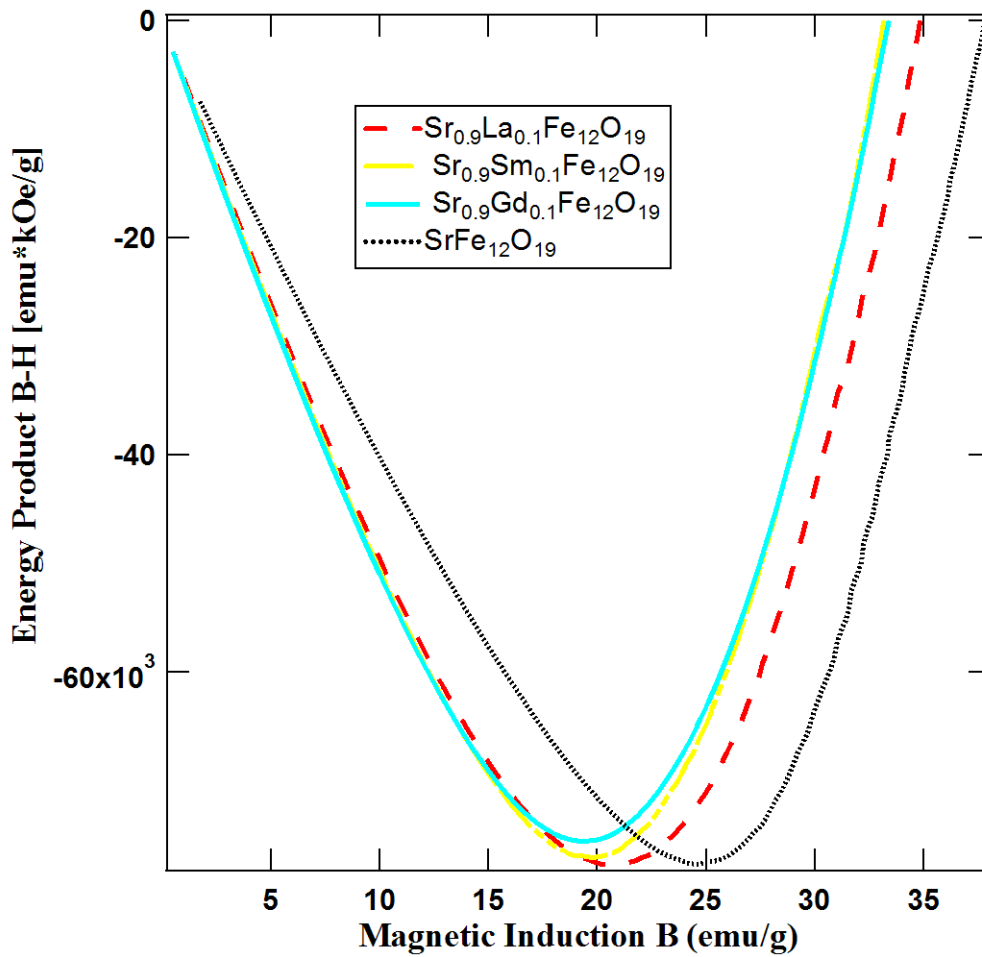
Fig. 4.28 Energy product vs magnetic induction 'B' of $Sr_{0.9}RE_{0.1}Fe_{12}O_{19}$.

From Fig. 4.27 and Fig. 4.28, it is concluded that RE doping for Sr, brings in enhancement in the (BH) value, a quality desired from a better magnets.

4.5 Raman spectroscopy studies

Fig. 4.29 Raman spectroscopy of the series of Al doped $SrAl_xFe_{12-x}O_{19}$.

Fig. 4.29 shows the Raman spectroscopy of the series of samples Al doped Strontium hexagonal ferrite. From the Fig.ure we see that as the Al doping level increases, the peaks between 600 and 800 (cm^{-1}) varies form several small peaks to a wide peak. The peaks between 600 and 800 (cm^{-1}) indicates the Fe position of $4f_2$

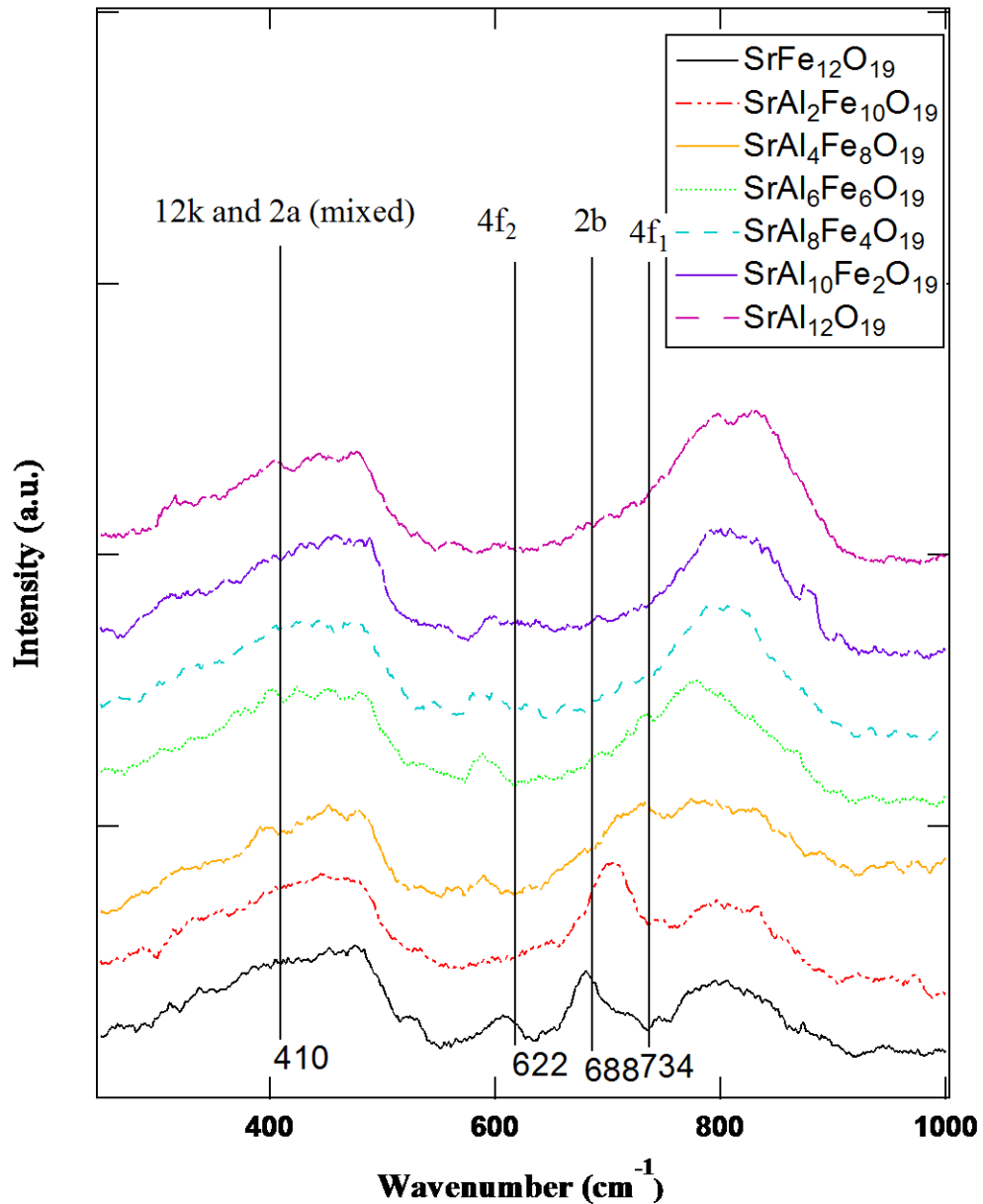(622 cm^{-1}), 2b (688 cm^{-1}), and $4f_1$ (738 cm^{-1}) [25]. It means the Al atom has succeeded in replacing the iron atoms in these positions. It can be obviously seen that the 2b site peak first shift to the right and then combain around $800 cm^{-1}$. It is easy to predict that the Al^{3+} ions will replace the 2b site Fe^{3+} ions first, which will cause the $Fe^{3+} - O - Fe^{3+}$ superexchange interaction weaker, leading to *Ms* reduction.

Raman spectroscopy of the La doped $Sr_{1-x}La_xFe_{12}O_{19}$ is shown in Fig. 4.30. The Raman spectra are nearly the same. Because the low rate of substitution, it is hard to see any change. However, when the level of substitution increases, the peak around $4f_2$ (622 cm^{-1}) appears to be lower, while the peak around $4f_1$ becomes stronger. It is because when we substitute more RE ions, the unit cell shrinks more on x axis. This affects the movement of iron ions on $4f_1$ and $4f_2$ sites.
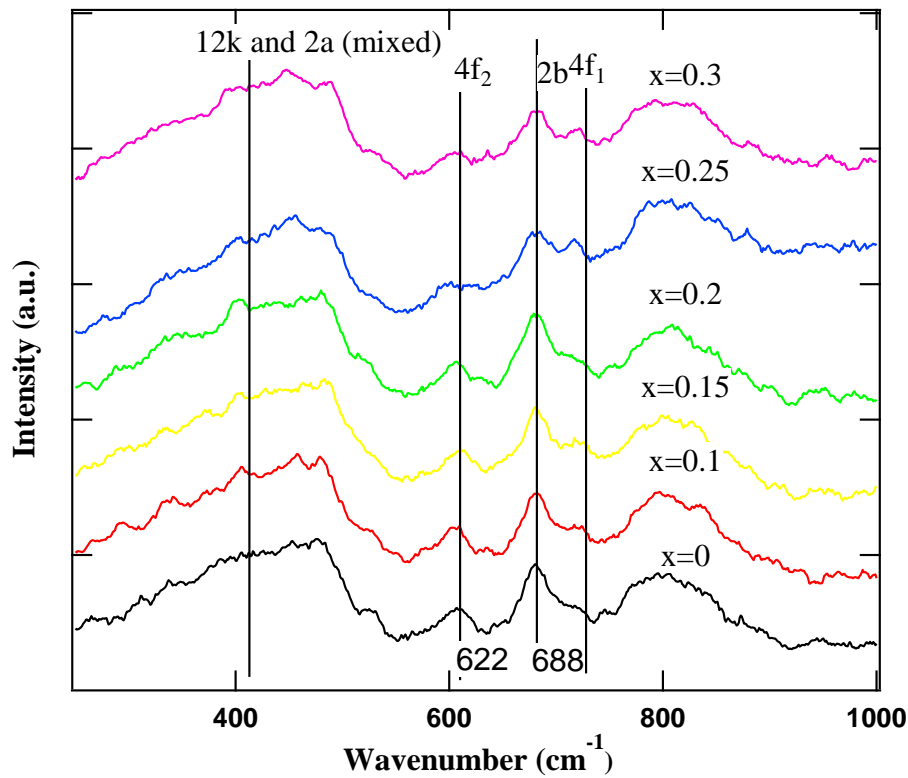

Fig. 4.30 Raman spectroscopy of the series of samples La doped $Sr_{1-x}La_xFe_{12}O_{19}$.

Raman spectra of RE ion substituted $Sr_{0.9}Re_{0.1}Fe_{12}O_{19}$ is shown in the Fig. 4.31.

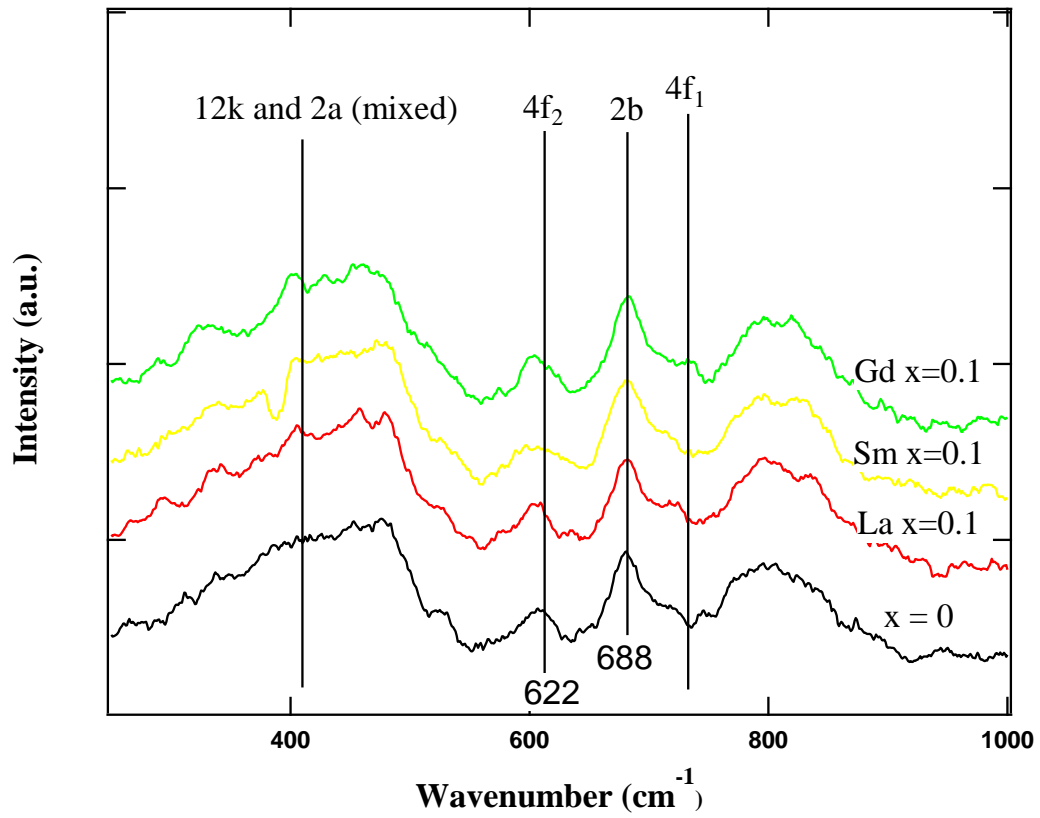Overall no perceptible changes in Raman intensity has been observed.

Fig. 4.31 Raman spectroscopy of the series of rare-earth ion doped $Sr_{0.9}Re_{0.1}Fe_{12}O_{19}$.

Chapter 5 Conclusion

The Aluminium doped M-type Strontium ferrite nanoparticles with a diameter about 100 nm was successfully prepared by sol-gel combustion method. With the Al^{3+} ions substitution, the lattice parameters and the crystallite sizes are found to decrease. The particle shape are observed to change from small spheres to needles. When the non-magnetic Al^{3+} ions replace the Fe^{3+} ions, the super-exchange interactions will be suppressed, so the magnetization of the nanoparticles reduces because the magnetic collinearity breaks down. Curie temperature is also found to decrease with Al doping because of reduction in exchange interaction. From the Raman spectroscopy results, we predict that the Al^{3+} ions will first replace the Fe^{3+} ions at 2b sites and 12k sites, which are ferromagnetic sites.

For the RE doped M-type Strontium ferrite nanoparticles, the RE ions substitution can enhance the magnetic properties of the particles at a special doping level. Different RE substitution doesn't change the crystal structure but affect the overall magnetic properties. This is because different rare-earth atoms act differently in converting Fe^{3+} to Fe^{2+}, having different crystallite anisotropy.

References

[1]. www.irm.umn.edu/hg2m/hg2m_b/hg2m_b.html. Hitchhiker's Guide to Magnetism.

[2]. F. Kools, Science of Sintering, **17**, 1-12 (1985).

[3]. W. Ervens and H. Wilmesmier, in "Magnetic Material" Ullmann's Enclyclopedia of Industrial Chemistry, Eds. B. Elvers, S. Hawkins, G.Shulz, VCH Verlag GmbH, D. Wernheim, Germany, Fifth edition, **A16**, 1-51 (1990).

[4]. C. M. Fang, F. Kools, R. Metselaar, G. de With, and R. A. de Groot, Journal of Physics: Condensed Matter, **15**, 6229-6237 (2003).

[5]. F. K. Lotgering, P. R. Locher, and R. P. van Stapele, Journal of Physical Chemical Society, **41**, 481-484 (1980).

[6]. L. Lechevallier, J. M. Le Breton, A. Morel, and P. Tenaud, Journal of Physics: Condensed Matter, **20**, 175-203 (2008).

[7]. X. Liu, W. Zhong, S. Yang, Z. Yu, B. Gu, and Y. Du, Journal of Magnetism and Magnetic Materials, **238**, 207 (2002).

[8]. S. Ounnunkad, Solid State Commun. **138**, 472 (2006).

[9]. M.A. Bohlman, F. G. Jones, and F. E. Luborsky, Metals Handbook, Ninth edition, **3**, 615-639 (1980).

[10]. Y. Kato and T. Takei, U.S.Patents 1.976.230 and 1.997.193 (1937)

[11]. J. J. Went, G.W. Rathenau, E. W. Gorter, and G. W. Van Oosterhout, "Ferroxdure, A class of new permanent magnetic materials" Philips Techn. Rev., **3**, 94-197 (1980).

[12]. E. W. Gorter, G. W. Rathenau, and A. L. Stuyts, U.S.Patent 2, 762.777. (1956).

[13]. A. L. Stuyts, G. H. Weber, and G. W. Rathenau, "Ferroxdure Ⅱ and Ⅲ. Anisotropic Permanent Magnet Materials", Philips Technical Review., **16**, 141-148 (1954).

[14]. N. J. Shirtcliffe, S. Thompson, E. S.O'Keefe, S. Appleton, and C. C. Perry, Materials Research Bulletin, **42**, 281-287 (2007).

[15]. C. H. Lin, Z. W. Shih, T. S. Chin, M.L.Wang, and Y. C. Yu, IEEE Transaction on Magnetics, **26**, 15-17 (1990).

[16]. J. Wang, Q. Chen, S. Che, Journal of Magnetism and Magnetic Materials, **280**, 281-286 (2004).

[17]. X. Obradors, A. Collomb, M. Pernet, D. Samaras, and J. C. Joubert, Journal of Solid State Chemistry, **56**, 171 (1985).

[18]. X. Obradors, X. Solans, A. Collomb, D. Samaras, J.Rodriguez, M. Pernet, and M.Font-Altaba, Journal of Solid State Chemistry, **72**, 218-224 (1988).

[19]. J. Wang and C. Zeng, Journal of Crystal Growth, **270**, 729-722 (2004).

[20]. J. Jalli, Y. K. Hong, S. H. Gee, S. Bae, J. Lee, J. C. Sur, G. S. Abo, A. Lyle, S. I. Lee, and T. Mewes, IEEETRANSACTIONS Om MAGNETICS, **44**, 2978-2981 (2008).

[21]. A. Singh, S. B. Narang, K. Singh, O. P. Pandey, and R. K. Kontnala, Journal

of Ceramic processing Research., **11**, 241-249 (2010).

[22]. F. J. Berry, J. F. Marco, C. B. Ponton, and K. R. Whittle, Journal of Materials Science Letters, **20**, 431-434 (2001).

[23]. Kittel, C., Introduction to Solid State Physics, 8th edition, John Wiley and Sons, Inc, Newyork, Chapters.1, 11, 12.

[24]. J. Kreisel, G. Lucazeau, and H. Vincent, Journal of Solid State Chemistry, **137**, 127-137(1998).

[25]. A. Morel, J. M. Le Breton, J. Kresel, G. Wiesinger, F. Kools, and P. Tenaud, Journal of Magnetism and Magnetic Materials, **242-245**, 1045-1047 (2002).

[26]. S. R. Shinde, S. E. Lofland, C. S. Ganpule, S. M. Bhagat, S. B. Bhagat, S. B. Ogale, R. Ramesh, and T. Venkatesan, Applied Physics Letter, **74**, 594-596 (1999).

[27]. C. Surig, K. Hempel, and D. Bonnenberg, Applied Physics Letter, **63**, 2836 (1993).

[28]. Q.S. Zhang, Fundamentals of Inorganic materials Sciences, East China University of Science and Technology Press, Shanghai (2007).

[29]. S. Thompson, N. Shirtcliffe, E. O'Keefe, S. Appleton, and C. Perry, Journal of Magnetism and Magnetic Materials, **292**, 100-107 (2005).

[30]. M. Liu, X. Shen, F. Song, J. Xiang, and X. Meng, Journal of Solid State Chemistry, **184**, 871-876 (2011).

[31]. C. S. Lin, C. C. Hwang, T. H. Huang, G. P. Wang, and C. H. Peng, Materials Science Engineering B. **139**, 24-36 (2007).

[32]. L. Lechevallier, J. M. Le Breton, J. F. Wang, and I. R. Harris, Journal of Magnetism and Magnetic Materials, **269**, 207 (2004).

[33]. A. M. Van Diepen and F. K. Lotgering, Journal of Physics Chemistry Solids, **35**, 1641 (1974).

[34]. X. Liu, W. Zhong, S. Yang, Z. Yu, B. Gu, and Y. Du, Physics Status Solidi A, **193**, 314 (2002).

[35]. Z. F. Zi, Y. P. Sun, X. B. Zhu, Z. R. Yang, J. M. Dai, and W. H. Song, Journal of Magnetism and Magnetic Materials, **320**, 2746-2751 (2008).

[36]. S. Chaudhury, S. K. Rakshit, S. C. Parida, Z. Singh, K. D. Singh Mudher, and V. Venugopal, Journal of Alloys and Compounds, **455**, 25-30 (2008).

[37]. B. Boyanov, Journal of the University of Chemical Technology and Metallurgy, **141**, 61-64 (2006).

[39]. Y. Huang, Z. Du, and X. Q, W. H, Chinese Journal of Materials Research, **21**, No.3 (2007).

[40]. T. H. Ting and K. H. Wu, Journal of Magnetism and Magnetic Materials, **322**, 2160-2166 (2010).